

# MAESTRO: Masked AutoEncoders for Multimodal, Multitemporal, and Multispectral Earth Observation Data

Antoine Labatie<sup>1</sup> Michael Vaccaro<sup>1</sup> Nina Lardiere<sup>1</sup> Anatol Garioud<sup>1</sup> Nicolas Gonthier<sup>1,2</sup>

<sup>1</sup> Institut national de l’information géographique et forestière (IGN), France

<sup>2</sup> Univ Gustave Eiffel, ENSG, IGN, LASTIG, France

{firstname.lastname}@ign.fr

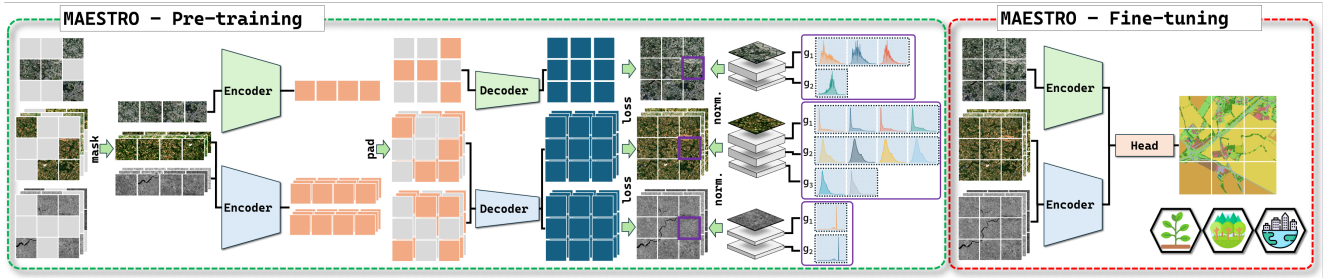


Figure 1. **Overview of MAESTRO.** MAESTRO extends the Masked Autoencoder to orchestrate the complex interplay of multimodal, multitemporal, and multispectral Earth Observation data. It employs token-based early fusion across time steps and similar modalities, and token-based late fusion across dissimilar modalities. It uses joint-token fusion for multispectrality, but still relies on a novel normalization of reconstruction targets—namely, patch-group-wise within groups of highly correlated bands—to inject a useful spectral prior during pretraining. Best viewed in color.

## Abstract

*Self-supervised learning holds great promise for remote sensing, but standard self-supervised methods must be adapted to the unique characteristics of Earth observation data. We take a step in this direction by conducting a comprehensive benchmark of fusion strategies and reconstruction target normalization schemes for multimodal, multitemporal, and multispectral Earth observation data. Based on our findings, we propose MAESTRO, a novel adaptation of the Masked Autoencoder, featuring optimized fusion strategies and a tailored target normalization scheme that introduces a spectral prior as a self-supervisory signal. Evaluated on four Earth observation datasets, MAESTRO sets a new state-of-the-art on tasks that strongly rely on multitemporal dynamics, while remaining highly competitive on tasks dominated by a single monotemporal modality. Code to reproduce all our experiments is available at <https://github.com/ignf/maestro>.*

## 1. Introduction

Self-supervised learning (SSL) has been central to recent breakthroughs in natural language processing [16, 63] and

computer vision [34, 96]. It is an effective pre-training strategy, improving versatility and data efficiency when fine-tuning models on diverse downstream tasks—especially in the case of foundation models pre-trained on large amounts of unlabeled data.

The SSL paradigm is promising for Earth Observation (EO) applications, where unlabeled data is abundant, but labeled data remains scarce and costly. However, to fully leverage the potential of SSL, it may be necessary to adapt off-the-shelf approaches to the unique characteristics of EO data. A key characteristic of EO data lies in its heterogeneity across resolutions, scales, modalities, and spectral bands [65]. This heterogeneity is frequently reflected in multimodal, multitemporal, and multispectral EO datasets, where the integration of various sensors effectively addresses the spatial-temporal-spectral “resolution dilemma” [2].

Our goal in this work is to efficiently adapt the canonical SSL framework of masked autoencoding to the specific characteristics of EO data to learn useful and versatile representations. We adapt the Masked Autoencoder (MAE) [34], which has shown strong performance and computational efficiency on natural images. However, extending the MAE to multimodal, multitemporal, and multispectral EO data introduces several challenges. First, integrating multiple

modalities and temporal observations requires an effective fusion strategy. One approach, *joint-token fusion*, projects all data dimensions into a shared token space. An alternative, *token-based fusion*, first clusters data dimensions, embeds them separately, and fuses the resulting tokens.

Token-based fusion appears more suited for handling multimodality and multitemporality for several reasons: (i) it better captures the heterogeneity across modalities and time steps, (ii) it allows the integration of modality- and temporality-specific encodings, and (iii) it enables the use of cross-modal and cross-temporal self-supervisory signals. Yet, it remains unclear whether fusion should be applied early or late in the model.

Second, handling multispectral data adds further complexity. Here, the choice between token-based and joint-token fusion is less obvious. While joint-token fusion offers computational efficiency, it limits the ability to incorporate cross-spectral self-supervisory signals. A key question, then, is whether we can preserve the computational benefits of joint-token fusion while reintroducing an effective prior on the multispectral structure—potentially through a carefully designed normalization of reconstruction targets.

We investigate these questions in Sec. 4.3 and, based on our findings, introduce our proposed approach, **MAESTRO**, in Sec. 4.4. MAESTRO extends the MAE framework by applying token-based early fusion across time steps and similar modalities, and token-based late fusion across dissimilar modalities. For multispectrality, MAESTRO employs joint-token early fusion combined with a novel normalization scheme for reconstruction targets.

Our main contributions are as follows:

- We extensively benchmark various fusion strategies and target normalization schemes for multimodal, multitemporal, and multispectral SSL in EO.
- We introduce a novel patch-group-wise normalization method that normalizes reconstruction targets patch-wise within groups of highly correlated spectral bands. This approach injects a useful spectral prior into the self-supervised signal at negligible computational cost.
- Building on the above, we propose MAESTRO, a tailored adaptation of the MAE framework which effectively orchestrates the use of multimodal, multitemporal, and multispectral EO data—both in terms of performance and computational cost.
- We validate MAESTRO on four diverse EO benchmarks, demonstrating that it achieves state-of-the-art results on tasks strongly tied to multitemporal dynamics, while remaining highly competitive on others.

## 2. Related Work

**SSL Approaches and Models for EO.** SSL has emerged as a promising approach for EO, due to the abundance of unlabeled remote sensing data. Initially, the development of

SSL approaches for EO followed those from the natural images domain. Early work focused primarily on contrastive SSL [6, 14, 39, 42, 52, 54, 61, 73, 88, 90, 91, 94], often using convolutional neural networks [6, 39, 52, 54, 61, 73, 90, 94]. Positive pairs were typically derived from different modalities, dates, or augmented views at the same location.

More recent works have increasingly shifted toward generative SSL using Transformers, well-suited to masked autoencoding. These include approaches inspired by MAE [9, 11, 13, 35, 37, 40, 48, 49, 58, 64, 71, 72, 77, 80, 83–86, 92, 93, 97, 100] or SimMIM [17, 33, 36, 55, 68, 70], or custom generative approaches [20, 21, 67, 87, 89]. Some recent works also explore hybrid contrastive/generative approaches [18, 57] or latent-space generative SSL [4, 5, 12, 45, 78, 82].

**Multimodal and Multitemporal SSL for EO.** Recent studies in EO have begun to address multimodal [8, 9, 14, 24, 33, 36, 37, 39, 41, 58, 61, 62, 82, 88, 90, 93, 97] or multitemporal SSL [13, 21, 40, 59, 71], but rarely both simultaneously. When multimodality is included, it is typically handled through parameter sharing or late fusion [7, 33, 37, 58, 62, 88, 93, 97]. To date, most published EO foundation models support multimodal or multitemporal inputs only via late fusion, which limits representation learning and downstream performance (see Sec. 4.3).

Notable exceptions include Presto [77], Galileo [78], OmniSat [4], AnySat [5], SeaMo [46], EarthMAE [80], SkySense v1/v2 [32, 101], and SkySense++ [95]. Among these, Presto processes data pixel-wise without spatial context; OmniSat and AnySat use joint-token early fusion (via LTAE [29]) across time steps; Galileo applies token-based early fusion across all time steps and modalities. In contrast, MAESTRO adopts token-based early fusion across time steps and similar modalities only, avoiding the inefficiencies of sharing encoders across dissimilar modalities. Despite the importance of fusion design in multimodal and multitemporal SSL (see Sec. 4.3), to our knowledge only one prior work [46] has benchmarked different fusion strategies—and even then, multitemporal fusion was limited to SSL pre-training and excluded fine-tuning evaluation.

**Multispectral SSL for EO.** Various SSL studies in EO have incorporated SAR [36, 42, 45, 49] or multispectral data [13, 15, 21, 37, 40, 54, 55, 62, 67, 68, 71, 73, 94] or both [4, 5, 7–9, 14, 24, 33, 39, 41, 43, 47, 58, 61, 77, 78, 80, 82, 88, 90–93, 97]. However, only a few have explicitly encoded spectral priors into the model architecture or the self-supervisory signal. Some prior works have used token-based multispectral fusion by assigning separate tokens to each spectral band [9, 62] or to groups of spectral bands [13, 37, 77, 78]. While these designs can help mitigate early information bottlenecks, enhance modeling capacity, and enable cross-spectral self-supervisory signals, they come at the cost of higher computational demands.

A handful of studies have explored the normalization of reconstruction targets for multispectral data, but their approaches have been restricted to patch-wise normalization without modeling the underlying spectral structure [58, 80]. In contrast, we normalize reconstruction targets across groups of highly correlated spectral bands, effectively injecting a spectral prior into the self-supervisory signal. This approach enhances spectral representation learning without increasing the token count and naturally extends to SAR inputs via analogous band-grouping strategies.

### 3. Approach

#### 3.1. Architecture

In this section, we describe our MAE-derived approach specifically tailored to EO data. Our approach accommodates the heterogeneous nature of EO data, notably its multimodal, multitemporal, and multispectral characteristics.

We describe our approach in the context of a fixed dataset  $\mathcal{D}$ , composed of a set of modalities  $m \in \mathcal{M}$ . For each dataset tile, every modality  $m$  is associated with an input tensor of shape  $I_m \times I_m \times T_m \times C_m$ , where  $I_m$  denotes the spatial size,  $T_m \geq 1$  the number of original time steps, and  $C_m$  the number of channels. We assume that  $C_m$  and  $I_m$  remain constant across all tiles, while  $T_m$  may vary. This variability reflects the nature of satellite time series, which may span a fixed duration but with location-dependent revisit intervals—such as with Sentinel-1 or Sentinel-2.

**Multitemporal Discretization.** Our preprocessing pipeline begins by enforcing a fixed tensor shape for the model inputs. For each modality  $m$ , we define a target number of discretized time steps  $D_m$ . For modality  $m$ , the original input tensor of shape  $I_m \times I_m \times T_m \times C_m$  is reduced to a tensor of shape  $I_m \times I_m \times D_m \times C_m$  through a two-step process: (i) temporal binning, where the sequence is reshaped into  $D_m$  bins, each covering  $T_m/D_m$  time steps (after a random truncation, if needed); and (ii) time step selection within each bin.

During training, time step selection within each bin is random to introduce data augmentation. During validation and testing, the selection aims to maximize the representativeness of each bin. For more information, refer to SM Sec. 6.2.1.

**Patchification/Unpatchification.** Once the inputs from different modalities have been reduced to a fixed shape, they are passed to modality-specific tokenizers. These tokenizers are shared across time steps within a given modality but remain distinct across modalities. Tokenization is applied independently at each time step.

We adopt the standard Vision Transformer (ViT) patchification strategy [19], where for any modality  $m$  and time step, inputs are first partitioned spatially into non-overlapping patches of size  $P_m$ . Each patch is then flat-

tened into a vector of shape  $P_m^2 C_m$  and projected into a patch embedding of dimension  $C_e$  before the encoder. All spectral bands are jointly projected into the same tokens, implementing *joint-token multispectral fusion*. During SSL pre-training, we apply transposed unpatchification to convert decoded tokens of shape  $C_d$  after the decoder back into reconstructed flattened patches of shape  $P_m^2 C_m$ .

For each modality  $m$ , the set of patch positions  $p \in \mathcal{P}_m$  has cardinality  $|\mathcal{P}_m| = (I_m/P_m)^2$ , while the set of temporal bins  $t \in \mathcal{T}_m$  has cardinality  $|\mathcal{T}_m| = D_m$ . Importantly, we do not assume that all modalities share the same number of spatial positions or temporal bins—that is, their spatial and temporal resolutions may differ. For example, modalities such as Sentinel-1 and Sentinel-2 may employ coarser spatial grids but finer temporal grids, whereas modalities such as aerial and SPOT 6–7 may use finer spatial grids with coarser temporal resolution. Maintaining these coarse or fine resolutions throughout the tokenization process helps prevent information bottlenecks in the tokenizers—the model’s entry blocks.

Following tokenization, we add (i) two-dimensional spatial positional encodings based on ground sampling distance, as in ScaleMAE [64], and (ii) sine-cosine temporal encodings, as used in SatMAE [13]. We do not include explicit modality encodings, as modality-specific tokenizers and learnable modality-specific [mask] tokens implicitly encode the source or target modality associated with each token. For more information, refer to SM Sec. 6.2.2.

#### Multimodal and Multitemporal Token-Based Fusion.

At this stage, we obtain embedded inputs in the form of tensors of shape  $I_m/P_m \times I_m/P_m \times D_m \times C_e$  for each modality  $m$ . As in the original MAE [34], these tensors are processed in two stages: a Transformer encoder processes only the visible tokens, while a Transformer decoder processes the encoded tokens concatenated with [mask] tokens.

However, the original MAE workflow was designed for monomodal, monotemporal data, and there remains ambiguity on how it should be extended to support multimodal and multitemporal data. This raises key questions:

- Should information from different modalities and time steps be fused via *early fusion* or *late fusion*?
- Should encoder and decoder parameters be shared across modalities or kept independent?

To answer these questions, we explore five different fusion modes, as illustrated in Fig. 2:

- Mode *shared*: Late fusion across modalities and time steps. Parameters are shared across all modalities.
- Mode *monotemp*: Same as *shared*, but with parameters kept independent for each modality.
- Mode *mod*: Late fusion across modalities but early fusion across time steps. Parameters are kept independent for each modality.

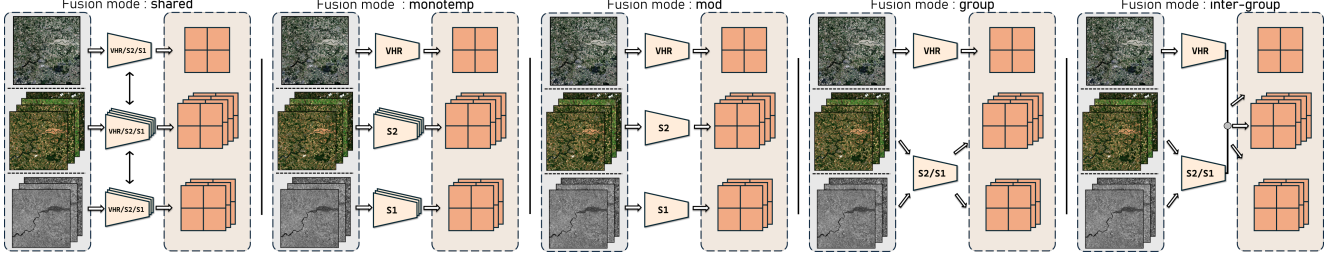


Figure 2. **Token-based fusion modes for handling multimodality and multitemporality.** Modes *shared* and *monotemp* involve late fusion across modalities and time steps, with parameters either shared across modalities (*shared*) or kept independent for each modality (*monotemp*). Mode *group* involves late fusion across predefined groups of modalities but early fusion across time steps and within each group. Mode *inter-group* extends *group* by replacing the final encoder blocks with fusion blocks that enable cross-group token interactions. Mode *mod* is a special case of *group* with late fusion across all modalities, but early fusion across time steps.

- **Mode *group*:** Late fusion across predefined groups of modalities but early fusion across time steps and within each group. Parameters are kept independent across groups.
- **Mode *inter-group*:** Similar to *group*, but with the last three encoder blocks replaced by fusion blocks enabling cross-group token interactions. Modalities from different groups are subject to intermediate fusion rather than late fusion.

Note that, strictly speaking, the term “late fusion” applies only to fine-tuning, where pooling occurs before the prediction heads. In SSL pre-training, no such pooling occurs before the decoder.

### 3.2. Pretext Task

**Multispectral Patch Normalization.** Our tokenizers jointly encode all spectral bands of each modality into shared tokens, implementing *joint-token multispectral fusion*. While this design improves efficiency, we still aim to embed meaningful spectral priors into the reconstruction task. To achieve this, we extend the *patch-wise* target normalization strategy, originally proposed in MAE [34] and later adopted in several EO-focused works [35, 58, 80, 83], with a *patch-group-wise* target normalization strategy. Specifically, for each modality  $m$ , we consider partitioning the spectral bands into a set of band groups  $g \in \mathcal{G}_m$ , and normalizing the targets independently for each patch and each band group.

Using the same notations as previously, let  $\mathbf{x}_m, \mathbf{x}_m^{\text{rec}} \in \mathbb{R}^{I_m/P_m \times I_m/P_m \times D_m \times P_m^2 C_m}$  denote the patch-level representations of unnormalized and reconstructed targets for modality  $m$ , respectively. The reconstruction loss—based on an  $L^1$  loss—then depends on the chosen normalization strategy:

- **No normalization:** Targets  $\mathbf{x}_m$  are used as-is:

$$\mathcal{L} = \frac{1}{\sum_m |\mathcal{P}_m| |\mathcal{T}_m|} \sum_{m,p,t} \|\mathbf{x}_{m,p,t} - \mathbf{x}_{m,p,t}^{\text{rec}}\|_1;$$

- **Patch-wise normalization:** Targets are normalized independently per patch across all bands [34, 35, 58, 80, 83]:

$$\hat{\mathcal{L}} = \frac{1}{\sum_m |\mathcal{P}_m| |\mathcal{T}_m|} \sum_{m,p,t} \|\hat{\mathbf{x}}_{m,p,t} - \mathbf{x}_{m,p,t}^{\text{rec}}\|_1,$$

$$\forall m, p, t: \quad \hat{\mathbf{x}}_{m,p,t} = \frac{\mathbf{x}_{m,p,t} - \mu(\mathbf{x}_{m,p,t})}{\sigma(\mathbf{x}_{m,p,t})};$$

- **Patch-group-wise normalization** (see Fig. 1): Targets are normalized independently per patch and band group:

$$\hat{\mathcal{L}}^{\text{grp}} = \frac{1}{\sum_m |\mathcal{P}_m| |\mathcal{T}_m| |\mathcal{G}_m|} \sum_{m,p,t,g} \|\hat{\mathbf{x}}_{m,p,t,g}^{\text{grp}} - \mathbf{x}_{m,p,t,g}^{\text{rec}}\|_1,$$

$$\forall m, p, t, g: \quad \hat{\mathbf{x}}_{m,p,t,g}^{\text{grp}} = \frac{\mathbf{x}_{m,p,t,g} - \mu(\mathbf{x}_{m,p,t,g})}{\sigma(\mathbf{x}_{m,p,t,g})}.$$

Our patch-group-wise target normalization generalizes the original patch-wise normalization; specifically, when all bands are grouped into a single set, it reduces to the original strategy used in [34, 35, 58, 80, 83].

We find that applying patch-group-wise normalization with well-chosen spectral groups  $g \in \mathcal{G}_m$ , composed of highly correlated bands, yields strong performance. As shown in Sec. 4.3, this target normalization allows joint-token fusion to match—and sometimes even surpass—the performance of token-based fusion, while being significantly more computationally efficient.

**Masking.** Another aspect that must be adapted to heterogeneous data is the masking strategy. Our goal is to maintain a fixed masking ratio within the token sets processed by each encoder and decoder. However, in the case of heterogeneous modalities, it remains ambiguous how this masking should be applied across the different token sets.

We choose a two-stage approach: (i) applying structured masking over modality, spatial, and temporal dimensions, and (ii) performing an unstructured adjustment to meet an overall masking ratio of 75%. Full details and comparisons with masking strategies from previous works are given in SM Sec. 6.3.1.



### 3.3. Downstream Tasks

**Classification/Segmentation Heads.** Following the MAE framework, we transfer only the encoders after SSL pre-training, mitigating domain shift effects related to [mask] tokens [16, 50].

As a result, the encoder outputs are feature tensors of shape  $I_m/P_m \times I_m/P_m \times D_m \times C_e$  for each modality  $m$ .

We then attach classification and segmentation heads to process these encoded features (see Fig. 1):

- *Classification heads* operate as follows:
  - (i) Concatenate tokens across all modalities  $m$ , spatial positions  $p$ , and time steps  $t$ ;
  - (ii) Apply attentive pooling [22] to aggregate the concatenated tokens;
  - (iii) Apply a dense layer with output dimension equal to the number of target classes.
- *Segmentation heads* first align all modality-specific encoded tensors to a common spatial *token grid of reference*. Then, for each spatial position  $p$ , they operate as follows:
  - (i) Concatenate tokens across all modalities  $m$  and time steps  $t$ ;
  - (ii) Apply attentive pooling to aggregate the concatenated tokens;
  - (iii) Apply a dense layer with output dimension equal to the number of target classes.

## 4. Experiments

### 4.1. Workflow

Our workflow varies depending on the evaluated models.

With MAEs, we follow a three-phase workflow applied sequentially on the same dataset:

1. **Self-supervised pre-training:** The model learns representations from unlabeled data without supervision.
2. **Probing:** A task-specific head is trained on top of the frozen pre-trained backbone to assess the quality of the learned representations. Only the task-specific head’s parameters are updated in this phase.
3. **Fine-tuning:** The entire model—including both the backbone and the task-specific head—is trained end-to-end in a fully supervised manner.

With baseline foundation models (FMs) and supervised ViTs, we focus solely on the supervised fine-tuning phase, which is closer to an operational setting.

Note that our MAE workflow involves only intra-dataset transfer learning; inter-dataset transfer is not addressed in this work. Importantly, our SSL pre-training is performed exclusively on the union of the training and validation sets, with test sets strictly excluded. This ensures that the MAE models do not gain an unfair advantage through any form of prior exposure to the fine-tuning test domains, including indirectly via input modalities.

### 4.2. Datasets

We apply our workflows to four medium- to large-scale datasets involving multimodality, multitemporality, and multispectrality:

- **TreeSatAI-TS** [1, 4] – Tree species identification with 15 multi-label classes. The dataset comprises 50 381 tiles of  $60 \text{ m} \times 60 \text{ m}$  across Germany, with aerial imagery (RGB + NIR) at 0.2 m resolution, along with Sentinel-1 and Sentinel-2 time series covering the full year closest to the aerial acquisition.
- **PASTIS-HD** [4, 30] – Agricultural crop segmentation with 19 semantic classes. This dataset includes 433 tiles of  $1280 \text{ m} \times 1280 \text{ m}$  in France, with very high-resolution (VHR) satellite imagery (SPOT 6–7) resampled to 1 m, along with Sentinel-1 time series covering about 70 acquisitions in both ascending and descending orbits and Sentinel-2 time series spanning approximately one year.
- **FLAIR#2** [26, 27] – Land cover segmentation with 12 semantic classes. The dataset consists of 77 762 tiles of  $102.4 \text{ m} \times 102.4 \text{ m}$  in France, with aerial and elevation imagery (RGB + NIR + DSM) at 0.2 m resolution, along with Sentinel-2 time series spanning a full year. As in [5], we use a version of FLAIR#2 without super-patches, cropping the Sentinel-2 time series to the VHR image extent (discarding 93.5% of pixels).
- **FLAIR-HUB** [28] – Land cover segmentation with 15 semantic classes. This extended version of FLAIR#2 includes 241 100 tiles of  $102.4 \text{ m} \times 102.4 \text{ m}$  in France, with aerial and elevation imagery (RGB + NIR + DEM + DSM) at 0.2 m resolution, along with Sentinel-1 and Sentinel-2 time series covering a full year.

Note that we do not use the full set of labels or input modalities for some datasets (see SM Sec. 6.1 for details). To study scaling laws with respect to pre-training and fine-tuning dataset size, we also create filtered versions of each dataset containing 20% and 5% of the original samples. These subsets are obtained via Furthest Point Sampling based on geographical coordinates.

### 4.3. Ablation studies

In this section, we assess the impact of various choices of SSL strategy and model components to guide the design of our final approach. We conduct experiments on TreeSatAI-TS, PASTIS-HD (fold I), and FLAIR-HUB (filtered at 20%, using split 1). Our comparison includes MAE and ViT models [19], alongside several baseline FMs—DINO-v2 [60], DINO-v2 sat.[74], DOFA[97], and CROMA [24]—with hyperparameters carefully set after extensive tuning.

By default, we use the *group* fusion mode, grouping together the Sentinel-1 ascending and descending modalities. For multispectral data, we apply *joint-token* fusion with *patch-group-wise* target normalization during reconstruction, based on spectral band groups exhibiting strong intra-

group and weaker inter-group correlations across Sentinel-2, Sentinel-1, and aerial modalities. Full details are provided in SM Secs. 6.3 and 6.4.

**Multimodal and Multitemporal Fusion.** We evaluate in Fig. 3 and SM Tab. 11 the different multimodal and multitemporal fusion modes outlined in Fig. 2.

In terms of multimodal fusion, we observe a modest benefit from early fusion among similar modalities, but a significant performance drop when it is applied across dissimilar ones (“group” with all modalities grouped performs worst on all three datasets). Additionally, sharing encoder parameters across modalities did not consistently help when using late fusion (“monotemp” vs “shared”).

Overall, these results suggest that the potential benefits of synergistic learning across modalities may not outweigh the drawbacks of reduced modality-specific specialization. This finding—likely reflecting the strong heterogeneity of EO modalities—casts doubt on strategies aimed at building universal and modality-agnostic FMs for EO.

Regarding multitemporality, we find that early multitemporal fusion (“mod”, “group”, and “inter-group”) consistently outperforms late multitemporal fusion (“shared” and “monotemp”) by +2–3% on TreeSatAI-TS (weighted F1) and PASTIS-HD (mIoU), and +1% on FLAIR-HUB (mIoU). The performance gain is especially pronounced on tasks where temporal dynamics play a critical role (see SM Sec. 7.5). The benefit is also more significant for MAEs than for supervised ViTs, suggesting that effectively leveraging temporal dynamics is both essential and non-trivial.

These findings highlight a potentially overlooked opportunity in multitemporal SSL, which has received less attention than multimodal SSL in prior work. Notably, most existing FMs are inherently monotemporal and thus only compatible with late multitemporal fusion, resulting in a significant performance gap compared to models involving early multitemporal fusion.

**Multispectral Fusion and Target Normalization.** In Fig. 4 and SM Tab. 12, we evaluate different choices of multispectral fusion and target normalization. Here, we limit our evaluation to TreeSatAI-TS and PASTIS-HD (using fold I) since the performance on FLAIR-HUB is driven mainly by the aerial modality (see SM Sec. 7.6), which exhibits only a weak multispectral nature.

We first evaluate the impact of different choices of target normalization within joint-token fusion, where all spectral band groups are combined into the same tokens. Consistent with prior work [34, 35], patch-wise normalization improves performance, but our proposed patch-group-wise approach yields significantly better results. This normalization supports effective transfer learning, even when using only 20% or 5% of pre-training data, as shown in Fig. 4. Overall, our findings highlight that target normalization is essential to fully leverage larger pre-training datasets.

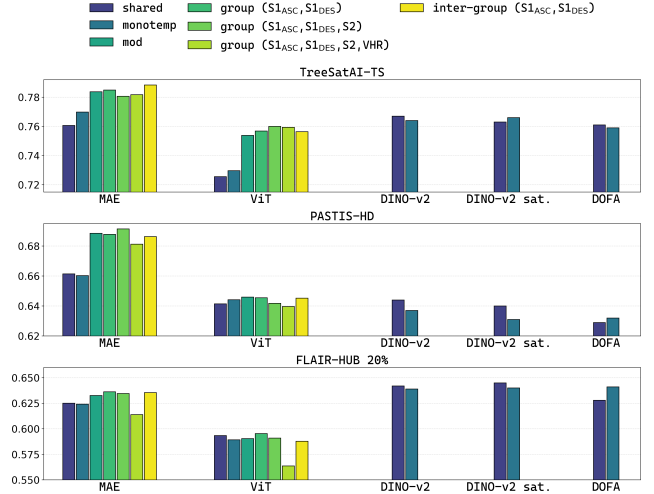


Figure 3. **Comparison of different multimodal and multitemporal fusion modes for MAEs, ViTs, and baseline FMs.** We report the weighted F1 score (%) on TreeSatAI-TS and the mIoU (%) on PASTIS-HD and FLAIR-HUB 20%. Refer to SM Tab. 11 for exact numbers and additional results with CROMA.

Strikingly, patch-group-wise normalization combined with joint-token fusion matches—and sometimes even surpasses—the performance of patch-wise normalization combined with token-based fusion, where each spectral band group forms a separate token [9, 13, 35, 37, 62, 77, 78]. With token-based fusion, patch-wise normalization naturally applies within each spectral group since each group corresponds to a distinct token, making the two approaches equivalent in terms of target normalization.

This result is especially notable given the computational implications: while token-based fusion incurs a cost that grows linearly with the number of spectral groups, patch-group-wise normalization combined with joint-token fusion achieves similar performance at negligible overhead.

To our knowledge, the underlying reason why patch-wise normalization improves performance remains unclear, even for SSL methods that reconstruct RGB images or videos [34, 75]. One hypothesis is that it helps balance the pretext task by ensuring uniform difficulty and loss contribution across patches.

However, patch-wise normalization may fail to provide such balance on multispectral EO data. For example, if different bands have narrow but non-overlapping histograms, patch-wise normalization tends to be equivalent to applying a constant normalization with no patch dependence. Patch-group-wise normalization addresses this by adapting normalization to both the patch and the spectral group.

We hypothesize that this balancing requirement is specific to pixel-space generative SSL. In contrast, latent-space generative SSL methods typically achieve balance implicit-

itly—by normalizing either before the loss [3] through layers such as LayerNorm, or within the loss via softmax [60, 82, 102] or cosine similarity [78].

Overall, our findings suggest that, for multispectral data, ensuring a balanced pretext task may be more important than using complex fusion strategies.

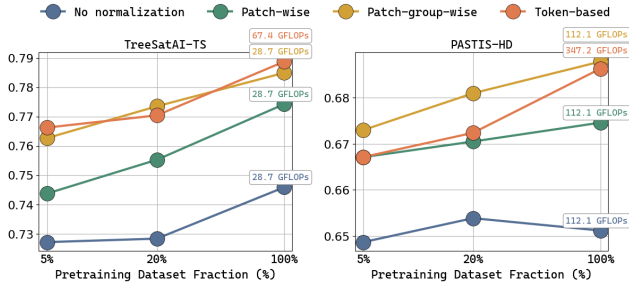


Figure 4. **Comparison of different choices of multispectral fusion and target normalization for MAE-B models.** We report the weighted F1 score (%) on TreeSatAI-TS and the mIoU (%) on PASTIS-HD, with varying pre-training dataset fractions. For each dataset and choice of multispectral fusion, we also indicate the pre-training cost in GFLOPs per forward pass (single batch element). Refer to SM Tab. 12 and Tab. 20 for exact numbers.

**Masking Strategy.** The evaluation of our masking strategy is provided in SM Sec. 7.4. In brief, the impact of the masking strategy is minor, though structured masking along each axis can yield noticeable benefits during probing.

#### 4.4. Design of MAESTRO

Following the analysis in Sec. 4.3, we finalize the choice of SSL strategy and model components for our new approach. We adopt either the *group* or the *inter-group* fusion mode, grouping together the Sentinel-1 ascending and descending modalities. This choice enables early fusion across time steps and across the Sentinel-1 modality pair, while enabling either intermediate or late fusion across other modality pairs. For multispectrality, we use *joint-token* fusion along with *patch-group-wise* target normalization during reconstruction.

We name our approach **MAESTRO** to reflect how it orchestrates the complex interplay of multimodal, multitemporal, and multispectral components in EO data within the MAE framework, as illustrated in Fig. 1.

#### 4.5. Performance

We evaluate in Tab. 1 the performance of MAESTRO alongside that of baseline FMs and supervised ViTs across the four evaluated datasets.

For supervised ViTs, we adopt either the *group* or *inter-group* fusion modes, grouping together the Sentinel-1 ascending and descending modalities, as done for MAESTRO. For baseline FMs, guided by the results in Fig. 3

and SM Tab. 11, we select the *shared* fusion mode, except for CROMA, where we use the *inter-croma* mode (see SM Sec. 6.4.3). As noted earlier, the baseline FMs have been extensively fine-tuned via hyperparameter search to ensure a fair comparison (see SM Sec. 6.4).

**MAESTRO vs. SOTA.** MAESTRO sets a new state-of-the-art (SOTA) on two of the evaluated datasets and nearly matches the previous SOTA or best-performing baseline FMs on the remaining two. Specifically, it outperforms the prior SOTA by **+2.7%** (weighted F1) on TreeSatAI-TS and by **+2.5%** (mIoU) on PASTIS-HD, while trailing by only -0.2% (mIoU) on FLAIR#2 and -0.1% (mIoU) on FLAIR-HUB compared to our adaptation of DINO-v2 (see SM Sec. 6.4.1), which sets the new SOTA on these two datasets.

**MAESTRO vs. Supervised ViTs.** MAESTRO outperforms supervised ViTs by even larger margins: **+3.7%** (weighted F1) on TreeSatAI-TS, **+4.4%** (mIoU) on PASTIS-HD, **+5.7%** (mIoU) on FLAIR#2, and **+3.8%** (mIoU) on FLAIR-HUB. Notably, MAESTRO maintains a strong advantage over ViTs even on the very large-scale FLAIR-HUB dataset, which is not always observed with other SSL methods [98]. Overall, these results suggest that transfer learning from SSL pre-training is essential to achieve good fine-tuning performance.

**MAESTRO vs. Baseline FMs.** MAESTRO significantly outperforms the baseline FMs on TreeSatAI-TS and PASTIS-HD, primarily due to the limitations of late multitemporal fusion—the only fusion strategy supported by these baseline FMs—which is particularly suboptimal for these datasets (see SM Sec. 7.5). However, this advantage does not extend to FLAIR#2 and FLAIR-HUB, where MAESTRO performs on par with, or slightly below, the best-performing baseline FMs. This is likely due to these datasets relying predominantly on the monotemporal aerial imagery (see SM Sec. 7.6), reducing the impact of the choice of multitemporal fusion.

Other factors influencing this comparison may counterbalance each other. For example, baseline FMs are often pre-trained on larger, more balanced datasets [60] using more computationally intensive methods. Yet, differences in pre-training modalities or preprocessing pipelines relative to fine-tuning can limit transfer effectiveness.

Interestingly—and perhaps unsurprisingly—baseline FMs perform best when the dominant modality in the fine-tuning dataset closely match those used during pre-training (see Tab. 1 and SM Tab. 3).

**Scaling by Dataset Size.** In Fig. 5 and SM Tab. 14, we finally assess the performance of MAESTRO and supervised ViTs across varying pre-training and fine-tuning dataset fractions. MAESTRO consistently outperforms supervised ViTs, especially when fine-tuning data is limited. Compar-

Table 1. **Performance comparison of MAESTRO, baseline FMs and supervised ViTs across the four evaluated datasets.** We report the weighted F1 score (%) on TreeSatAI-TS and the mIoU (%) on PASTIS-HD, FLAIR#2, and FLAIR-HUB. Arrows ( $\uparrow$  /  $\downarrow$ ) show the gains/losses versus the best other FM/ViT/SOTA. We have trained all models listed in this table except AnySat and previous SOTA (\*). MAESTRO<sup>†</sup> models have been pre-trained for twice the number of epochs.

Model	Model size	Fusion mode	TreeSatAI-TS	PASTIS-HD fold I	FLAIR#2 split 1	FLAIR-HUB split 1
MAESTRO (ours)	Base	group	78.5	68.8	63.8	64.9
MAESTRO (ours)	Base	inter-group	78.8	68.6	62.6	<b>65.9</b> $\downarrow 0.1$
MAESTRO (ours) <sup>†</sup>	Base	group	79.1	68.8	<b>64.0</b> $\downarrow 0.2$	64.8
MAESTRO (ours) <sup>†</sup>	Base	inter-group	<b>79.4</b> $\uparrow 2.7$	<b>69.0</b> $\uparrow 2.5$	63.3	65.8
DINO-v2 [60]	Base	shared	<b>76.7</b>	64.4	<b>64.2</b>	<b>66.0</b>
DINO-v2 sat. [74]	Large	shared	76.3	64.0	63.5	<b>66.0</b>
DOFA [97]	Base	shared	76.0	62.9	62.3	65.1
CROMA [24]	Base	inter-croma	70.5	65.0	39.0	44.3
AnySat* [5]	Base		75.1	<b>66.5</b>	55.1	
ViT	Base	group	<b>75.7</b>	<b>64.6</b>	<b>58.3</b>	61.6
ViT	Base	inter-group	75.6	64.5	58.2	<b>62.1</b>
Previous SOTA*			75.1 [5]	66.5 [5]	64.1 [69]	64.3 [28]

ing full and reduced pre-training datasets, we see that more unlabeled data systematically improves downstream performance regardless of the amount of labeled fine-tuning data.

These results suggest MAESTRO could further benefit from larger-scale unlabeled pre-training. However, fully leveraging such large-scale datasets may require additional balancing strategies—beyond our target normalization—tailored for large pretext tasks [42, 81].

## 5. Conclusion

In this work, we explored how to adapt SSL approaches to the distinctive characteristics of EO data, focusing on three axes of heterogeneity: multimodality, multitemporality, and multispectrality.

(i) **Multimodality** – Early fusion offers slight benefits when modalities are similar but can hurt performance when they differ significantly, raising doubts about the viability of universal, modality-agnostic EO foundation models. (ii) **Multitemporality** – Early fusion consistently outperforms late fusion for tasks that strongly rely on multitemporal dynamics, revealing an underexplored opportunity in multitemporal SSL. Current foundation models, being inherently monotemporal, are limited to late multitemporal fusion during fine-tuning, which can incur significant performance drops. (iii) **Multispectrality** – Joint-token early fusion combined with a proper target normalization for reconstruction matches the performance of token-based fusion while being significantly more efficient.

Building on these findings, we proposed **MAESTRO**—an adaptation of the MAE that effectively orchestrates the use of multimodal, multitemporal, and multispectral data in EO. Evaluated on four EO benchmarks, MAESTRO achieves SOTA results on tasks that strongly rely on

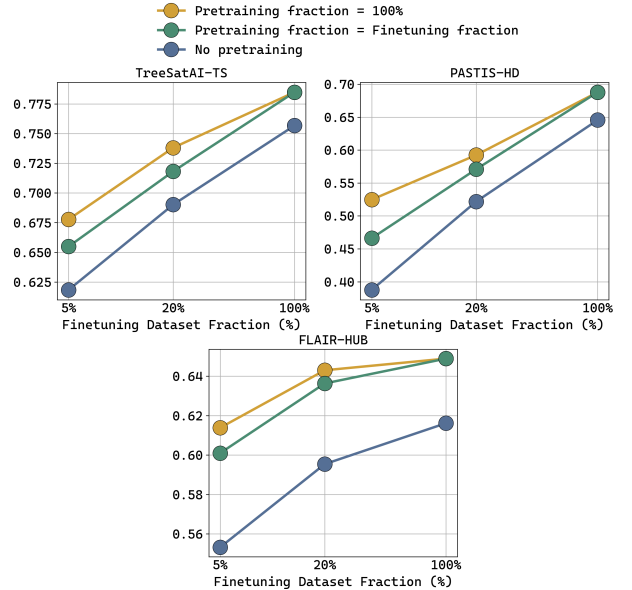


Figure 5. **Scaling of MAESTRO-B and ViT-B models with different pre-training/fine-tuning dataset fractions.** We report the weighted F1 score (%) on TreeSatAI-TS and the mIoU (%) on PASTIS-HD and FLAIR-HUB for three finetuning dataset fractions: 5%, 20%, and 100%. For each finetuning fraction, we compare three pre-training settings: pre-training on 100% of the data, pre-training on the same fraction as fine-tuning, and no pre-training. Refer to SM Tab. 14 for exact numbers.

temporal dynamics, while remaining highly competitive on others.

We hope that our work will contribute to the design of SSL strategies that specifically account for the distinctive characteristics of EO data.



## Acknowledgement

This work was granted access to the HPC/AI resources provided by GENCI-IDRIS (allocations A0181013803, A0161013803, and AD010114597R1). We thank SIMV/SDM colleagues at IGN, Guillaume Astruc, Loïc Landrieu, Alexandre Tuel, and Thomas Kerdreux for useful discussions.

## References

- [1] S. Ahlswede, C. Schulz, C. Gava, P. Helber, B. Bischke, M. Förster, F. Arias, J. Hees, B. Demir, and B. Kleinschmit. TreeSatAI benchmark archive: a multi-sensor, multi-label dataset for tree species classification in remote sensing. *Earth System Science Data*, 15(2):681–695, 2023. 5, 14
- [2] Firouz A Al-Wassai and NV Kalyankar. Major limitations of satellite images. *Journal of Global Research in Computer Science*, 4(5):51–59, 2013. 1
- [3] Mahmoud Assran, Quentin Duval, Ishan Misra, Piotr Bojanowski, Pascal Vincent, Michael Rabbat, Yann LeCun, and Nicolas Ballas. Self-supervised learning from images with a joint-embedding predictive architecture. In *Proceedings of the IEEE/CVF Conference on Computer Vision and Pattern Recognition*, pages 15619–15629, 2023. 7
- [4] Guillaume Astruc, Nicolas Gonthier, Clement Mallet, and Loïc Landrieu. OmniSat: Self-supervised modality fusion for earth observation. In *European Conference on Computer Vision (ECCV)*, pages 409–427. Springer, 2024. 2, 5, 14
- [5] Guillaume Astruc, Nicolas Gonthier, Clement Mallet, and Loïc Landrieu. AnySat: An earth observation model for any resolutions, scales, and modalities. In *Proceedings of the IEEE/CVF international conference on computer vision (CVPR)*, 2025. 2, 5, 8, 14, 18
- [6] Kumar Ayush, Burak Uzket, Chenlin Meng, Kumar Tanmay, Marshall Burke, David Lobell, and Stefano Ermon. Geography-aware self-supervised learning. In *Proceedings of the IEEE/CVF International Conference on Computer Vision*, pages 10181–10190, 2021. 2
- [7] Favyen Bastani, Piper Wolters, Ritwik Gupta, Joe Ferdinando, and Aniruddha Kembhavi. SatlasPretrain: A large-scale dataset for remote sensing image understanding. In *Proceedings of the IEEE/CVF International Conference on Computer Vision*, pages 16772–16782, 2023. 2
- [8] Hanbo Bi, Yingchao Feng, Boyuan Tong, Mengyu Wang, Haichen Yu, Yongqiang Mao, Hao Chang, Wenhui Diao, Peijin Wang, Yue Yu, et al. RingMoE: Mixture-of-modality-experts multi-modal foundation models for universal remote sensing image interpretation. *arXiv preprint arXiv:2504.03166*, 2025. 2
- [9] Nikolaos Ioannis Bountos, Arthur Ouaknine, Ioannis Papoutsis, and David Rolnick. FoMo: Multi-modal, multi-scale and multi-task remote sensing foundation models for forest monitoring. In *Proceedings of the AAAI Conference on Artificial Intelligence*, pages 27858–27868, 2025. 2, 6, 17
- [10] Mathilde Caron, Hugo Touvron, Ishan Misra, Hervé Jégou, Julien Mairal, Piotr Bojanowski, and Armand Joulin. Emerging properties in self-supervised vision transformers. In *Proceedings of the IEEE/CVF international conference on computer vision*, pages 9650–9660, 2021. 17
- [11] Keumgang Cha, Junghoon Seo, and Taekyung Lee. A billion-scale foundation model for remote sensing images. *arXiv preprint arXiv:2304.05215*, 2023. 2
- [12] Shabnam Choudhury, Yash Salunkhe, Sarthak Mehrotra, and Biplab Banerjee. REJEPa: A novel joint-embedding predictive architecture for efficient remote sensing image retrieval. In *Proceedings of the Computer Vision and Pattern Recognition Conference*, pages 2373–2382, 2025. 2
- [13] Yezhen Cong, Samar Khanna, Chenlin Meng, Patrick Liu, Erik Rozi, Yutong He, Marshall Burke, David Lobell, and Stefano Ermon. SatMAE: Pre-training transformers for temporal and multi-spectral satellite imagery. *Advances in Neural Information Processing Systems*, 35:197–211, 2022. 2, 3, 6, 17, 18
- [14] Muhammad Sohail Danish, Muhammad Akhtar Munir, Syed Roshan Ali Shah, Muhammad Haris Khan, Rao Muhammad Anwer, Jorma Laaksonen, Fahad Shahbaz Khan, and Salman Khan. TerraFM: A scalable foundation model for unified multisensor earth observation. *arXiv preprint arXiv:2506.06281*, 2025. 2
- [15] Rangel Daroya, Elijah Cole, Oisín Mac Aodha, Grant Van Horn, and Subhansu Maji. WildSAT: Learning satellite image representations from wildlife observations. *arXiv preprint arXiv:2412.14428*, 2024. 2
- [16] Jacob Devlin, Ming-Wei Chang, Kenton Lee, and Kristina Toutanova. BERT: Pre-training of deep bidirectional transformers for language understanding. In *Proceedings of the 2019 conference of the North American chapter of the association for computational linguistics: human language technologies, volume 1 (long and short papers)*, pages 4171–4186, 2019. 1, 5
- [17] Wenhui Diao, Haichen Yu, Kaiyue Kang, Tong Ling, Di Liu, Yingchao Feng, Hanbo Bi, Libo Ren, Xuexue Li, Yongqiang Mao, et al. RingMo-Aerial: An aerial remote sensing foundation model with a affine transformation contrastive learning. *arXiv preprint arXiv:2409.13366*, 2024. 2
- [18] Philipe Dias, Aristeidis Tsaris, Jordan Bowman, Abhishek Potnis, Jacob Arndt, H Lexie Yang, and Dalton Lungu. OReole-FM: successes and challenges toward billion-parameter foundation models for high-resolution satellite imagery. In *Proceedings of the 32nd ACM International Conference on Advances in Geographic Information Systems*, pages 597–600, 2024. 2
- [19] Alexey Dosovitskiy, Lucas Beyer, Alexander Kolesnikov, Dirk Weissenborn, Xiaohua Zhai, Thomas Unterthiner, Mostafa Dehghani, Matthias Minderer, Georg Heigold, Sylvain Gelly, Jakob Uszkoreit, and Neil Houlsby. An image is worth 16x16 words: Transformers for image recognition at scale. In *International Conference on Learning Representations*, 2021. 3, 5, 19
- [20] Chuc Man Duc and Hiromichi Fukui. SatMamba: Development of foundation models for remote sensing imagery us-

ing state space models. *arXiv preprint arXiv:2502.00435*, 2025. 2

- [21] Iris Dumeur, Silvia Valero, and Jordi Inglada. Self-supervised spatio-temporal representation learning of satellite image time series. *IEEE Journal of Selected Topics in Applied Earth Observations and Remote Sensing*, PP:1–18, 2024. 2
- [22] Alaaeldin El-Nouby, Michal Klein, Shuangfei Zhai, Miguel Ángel Bautista, Vaishaal Shankar, Alexander T Tsohe, Joshua M. Susskind, and Armand Joulin. Scalable pre-training of large autoregressive image models. In *Proceedings of the 41st International Conference on Machine Learning*, pages 12371–12384, 2024. 5
- [23] Fajwel Fogel, Yohann Perron, Nikola Besic, Laurent Saint-André, Agnès Pellissier-Tanon, Martin Schwartz, Thomas Boudras, Ibrahim Fayad, Alexandre d’Aspremont, Loic Landrieu, et al. Open-Canopy: Towards very high resolution forest monitoring. In *Proceedings of the Computer Vision and Pattern Recognition Conference*, pages 1395–1406, 2025. 19
- [24] Anthony Fuller, Koreen Millard, and James Green. CROMA: Remote sensing representations with contrastive radar-optical masked autoencoders. *Advances in Neural Information Processing Systems*, 36:5506–5538, 2023. 2, 5, 8, 19, 20, 23
- [25] Anatol Garioud, Stéphane Peillet, Eva Bookjans, Sébastien Giordano, and Boris Wattrélos. FLAIR# 1: semantic segmentation and domain adaptation dataset. *arXiv preprint arXiv:2211.12979*, 2022. 14
- [26] Anatol Garioud, Apolline De Wit, Marc Poupée, Marion Valette, Sébastien Giordano, and Boris Wattrélos. FLAIR# 2: textural and temporal information for semantic segmentation from multi-source optical imagery. *arXiv preprint arXiv:2305.14467*, 2023. 5, 14
- [27] Anatol Garioud, Nicolas Gonthier, Loic Landrieu, Apolline De Wit, Marion Valette, Marc Poupée, Sébastien Giordano, et al. FLAIR: a country-scale land cover semantic segmentation dataset from multi-source optical imagery. *Advances in Neural Information Processing Systems*, 36: 16456–16482, 2023. 5, 14
- [28] Anatol Garioud, Sébastien Giordano, Nicolas David, and Nicolas Gonthier. FLAIR-HUB: Large-scale multimodal dataset for land cover and crop mapping. *arXiv preprint arXiv:2506.07080*, 2025. 5, 8, 14, 15
- [29] Vivien Sainte Fare Garnot and Loic Landrieu. Lightweight temporal self-attention for classifying satellite images time series. In *Advanced Analytics and Learning on Temporal Data: 5th ECML PKDD Workshop, AALTD 2020, Ghent, Belgium, September 18, 2020, Revised Selected Papers 6*, pages 171–181. Springer, 2020. 2
- [30] Vivien Sainte Fare Garnot and Loic Landrieu. Panoptic segmentation of satellite image time series with convolutional temporal attention networks. In *Proceedings of the IEEE/CVF International Conference on Computer Vision*, pages 4872–4881, 2021. 5, 14
- [31] Vivien Sainte Fare Garnot, Loic Landrieu, and Nesrine Chehata. Multi-modal temporal attention models for crop mapping from satellite time series. *ISPRS Journal of Photogrammetry and Remote Sensing*, 187:294–305, 2022. 14
- [32] Xin Guo, Jiangwei Lao, Bo Dang, Yingying Zhang, Lei Yu, Lixiang Ru, Liheng Zhong, Ziyuan Huang, Kang Wu, Dingxiang Hu, et al. SkySense: A multi-modal remote sensing foundation model towards universal interpretation for earth observation imagery. In *Proceedings of the IEEE/CVF Conference on Computer Vision and Pattern Recognition*, pages 27672–27683, 2024. 2
- [33] Boran Han, Shuai Zhang, Xingjian Shi, and Markus Reichstein. Bridging remote sensors with multisensor geospatial foundation models. In *Proceedings of the IEEE/CVF Conference on Computer Vision and Pattern Recognition*, pages 27852–27862, 2024. 2
- [34] Kaiming He, Xinlei Chen, Saining Xie, Yanghao Li, Piotr Dollár, and Ross B. Girshick. Masked autoencoders are scalable vision learners. *2022 IEEE/CVF Conference on Computer Vision and Pattern Recognition (CVPR)*, pages 15979–15988, 2021. 1, 3, 4, 6, 16, 17
- [35] Danfeng Hong, Bing Zhang, Xuyang Li, Yuxuan Li, Chenyu Li, Jing Yao, Naoto Yokoya, Hao Li, Pedram Ghamisi, Xiuping Jia, et al. SpectralGPT: Spectral remote sensing foundation model. *IEEE Transactions on Pattern Analysis and Machine Intelligence*, 2024. 2, 4, 6
- [36] Huiyang Hu, Peijin Wang, Hanbo Bi, Boyuan Tong, Zhaozhi Wang, Wenhui Diao, Hao Chang, Yingchao Feng, Ziqi Zhang, Yaowei Wang, et al. RS-vHeat: Heat conduction guided efficient remote sensing foundation model. *arXiv preprint arXiv:2411.17984*, 2024. 2
- [37] Jeremy Irvin, Lucas Tao, Joanne Zhou, Yuntao Ma, Langston Nashold, Benjamin Liu, and Andrew Y Ng. USat: A unified self-supervised encoder for multi-sensor satellite imagery. *arXiv preprint arXiv:2312.02199*, 2023. 2, 6, 18
- [38] Pavel Izmailov, Dmitrii Podoprikin, Timur Garipov, Dmitry Vetrov, and Andrew Gordon Wilson. Averaging weights leads to wider optima and better generalization. In *Conference on Uncertainty in Artificial Intelligence (UAI)*, 2018. 17
- [39] Pallavi Jain, Bianca Schoen-Phelan, and Robert Ross. Self-supervised learning for invariant representations from multi-spectral and sar images. *IEEE Journal of Selected Topics in Applied Earth Observations and Remote Sensing*, 15:7797–7808, 2022. 2
- [40] Johannes Jakubik, Sujit Roy, CE Phillips, Paolo Fraccaro, Denys Godwin, Bianca Zadrozny, Daniela Szwarzman, Carlos Gomes, Gabby Nyirjesy, Blair Edwards, et al. Foundation models for generalist geospatial artificial intelligence. *arXiv preprint arXiv:2310.18660*, 2023. 2
- [41] Johannes Jakubik, Felix Yang, Benedikt Blumenstiel, Erik Scheurer, Rocco Sedona, Stefano Maurogiovanni, Jente Bosmans, Nikolaos Dionelis, Valerio Marsocci, Niklas Kopp, et al. TerraMind: Large-scale generative multimodality for earth observation. *arXiv preprint arXiv:2504.11171*, 2025. 2
- [42] Thomas Kerdreux, Alexandre Tuel, Quentin Febvre, Alexis Mouche, and Bertrand Chapron. Efficient self-supervised learning for earth observation via dynamic dataset curation.

- In *Proceedings of the Computer Vision and Pattern Recognition Conference (CVPR) Workshops*, pages 3017–3027, 2025. [2](#), [8](#)
- [43] Jingtao Li, Yingyi Liu, Xinyu Wang, Yunning Peng, Chen Sun, Shaoyu Wang, Zhendong Sun, Tian Ke, Xiao Jiang, Tangwei Lu, et al. HyperFree: A channel-adaptive and tuning-free foundation model for hyperspectral remote sensing imagery. In *Proceedings of the Computer Vision and Pattern Recognition Conference*, pages 23048–23058, 2025. [2](#)
- [44] Shuaipeng Li, Penghao Zhao, Hailin Zhang, Xingwu Sun, Hao Wu, Dian Jiao, Weiyan Wang, Chengjun Liu, Zheng Fang, Jinbao Xue, et al. Surge phenomenon in optimal learning rate and batch size scaling. *Advances in Neural Information Processing Systems*, 37:132722–132746, 2024. [17](#)
- [45] Weijie Li, Wei Yang, Tianpeng Liu, Yuenan Hou, Yuxuan Li, Zhen Liu, Yongxiang Liu, and Li Liu. Predicting gradient is better: Exploring self-supervised learning for sar atr with a joint-embedding predictive architecture. *ISPRS Journal of Photogrammetry and Remote Sensing*, 218:326–338, 2024. [2](#)
- [46] Xuyang Li, Danfeng Hong, Chenyu Li, and Jocelyn Chanussot. SeaMo: A multi-seasonal and multi-modal remote sensing foundation model. *arXiv preprint arXiv:2412.19237*, 2024. [2](#), [17](#)
- [47] Xuyang Li, Chenyu Li, Pedram Ghamisi, and Danfeng Hong. FlexiMo: A flexible remote sensing foundation model. *arXiv preprint arXiv:2503.23844*, 2025. [2](#)
- [48] Zhihao Li, Biao Hou, Siteng Ma, Zitong Wu, Xianpeng Guo, Bo Ren, and Licheng Jiao. Masked angle-aware autoencoder for remote sensing images. In *European Conference on Computer Vision*, pages 260–278. Springer, 2024. [2](#)
- [49] Junyan Lin, Feng Gao, Xiaochen Shi, Junyu Dong, and Qian Du. SS-MAE: Spatial-spectral masked autoencoder for multisource remote sensing image classification. *IEEE Transactions on Geoscience and Remote Sensing*, 61:1–14, 2023. [2](#)
- [50] Jihao Liu, Xin Huang, Jinliang Zheng, Yu Liu, and Hongsheng Li. MixMAE: Mixed and masked autoencoder for efficient pretraining of hierarchical vision transformers. In *Proceedings of the IEEE/CVF Conference on Computer Vision and Pattern Recognition*, pages 6252–6261, 2023. [5](#)
- [51] Ilya Loshchilov and Frank Hutter. Decoupled weight decay regularization. *arXiv preprint arXiv:1711.05101*, 2017. [17](#)
- [52] Utkarsh Mall, Bharath Hariharan, and Kavita Bala. Change-aware sampling and contrastive learning for satellite images. In *Proceedings of the IEEE/CVF Conference on Computer Vision and Pattern Recognition (CVPR)*, pages 5261–5270, 2023. [2](#)
- [53] Sadhika Malladi, Kaifeng Lyu, Abhishek Panigrahi, and Sanjeev Arora. On the sdes and scaling rules for adaptive gradient algorithms. *Advances in Neural Information Processing Systems*, 35:7697–7711, 2022. [17](#)
- [54] Oscar Manas, Alexandre Lacoste, Xavier Giró-i Nieto, David Vazquez, and Pau Rodriguez. Seasonal contrast: Unsupervised pre-training from uncured remote sensing data. In *Proceedings of the IEEE/CVF International Conference on Computer Vision*, pages 9414–9423, 2021. [2](#)
- [55] Matías Mendieta, Boran Han, Xingjian Shi, Yi Zhu, and Chen Chen. Towards geospatial foundation models via continual pretraining. In *Proceedings of the IEEE/CVF International Conference on Computer Vision*, pages 16806–16816, 2023. [2](#)
- [56] Daniel Morales-Brotons, Thijs Vogels, and Hadrien Hendrikx. Exponential moving average of weights in deep learning: Dynamics and benefits. *Transactions on Machine Learning Research*, 2024. [17](#), [22](#)
- [57] Dilxat Muhtar, Xueliang Zhang, Pengfeng Xiao, Zhenshi Li, and Feng Gu. CMID: A unified self-supervised learning framework for remote sensing image understanding. *IEEE Transactions on Geoscience and Remote Sensing*, 61:1–17, 2023. [2](#)
- [58] Vishal Nedungadi, Ankit Karirya, Stefan Oehmcke, Serge Belongie, Christian Igel, and Nico Lang. MMEarth: Exploring multi-modal pretext tasks for geospatial representation learning. In *European Conference on Computer Vision*, pages 164–182. Springer, 2024. [2](#), [3](#), [4](#)
- [59] Mubashir Noman, Muzammal Naseer, Hisham Cholakkal, Rao Muhammad Anwer, Salman Khan, and Fahad Shahbaz Khan. Rethinking transformers pre-training for multi-spectral satellite imagery. In *Proceedings of the IEEE/CVF Conference on Computer Vision and Pattern Recognition*, pages 27811–27819, 2024. [2](#)
- [60] Maxime Oquab, Timothée Darcet, Théo Moutakanni, Huy V. Vo, Marc Szafraniec, Vasil Khalidov, Pierre Fernandez, Daniel Haziza, Francisco Massa, Alaaeldin El-Nouby, Mido Assran, Nicolas Ballas, Wojciech Galuba, Russell Howes, Po-Yao Huang, Shang-Wen Li, Ishan Misra, Michael Rabbat, Vasu Sharma, Gabriel Synnaeve, Hu Xu, Herve Jegou, Julien Mairal, Patrick Labatut, Armand Joulin, and Piotr Bojanowski. DINOv2: Learning robust visual features without supervision. *Transactions on Machine Learning Research*, 2024. [5](#), [7](#), [8](#), [17](#), [19](#), [23](#)
- [61] Jonathan Prexl and Michael Schmitt. Multi-modal multi-objective contrastive learning for sentinel-1/2 imagery. In *Proceedings of the IEEE/CVF Conference on Computer Vision and Pattern Recognition (CVPR) Workshops*, pages 2136–2144, 2023. [2](#)
- [62] Jonathan Prexl and Michael Schmitt. SenPa-MAE: Sensor parameter aware masked autoencoder for multi-satellite self-supervised pretraining. In *DAGM German Conference on Pattern Recognition*, pages 317–331. Springer, 2024. [2](#), [6](#)
- [63] Alec Radford, Karthik Narasimhan, Tim Salimans, Ilya Sutskever, et al. Improving language understanding by generative pre-training. 2018. [1](#)
- [64] Colorado J Reed, Ritwik Gupta, Shufan Li, Sarah Brockman, Christopher Funk, Brian Clipp, Kurt Keutzer, Salvatore Candido, Matt Uyttendaele, and Trevor Darrell. ScaleMAE: A scale-aware masked autoencoder for multiscale geospatial representation learning. In *Proceedings of the IEEE/CVF International Conference on Computer Vision*, pages 4088–4099, 2023. [2](#), [3](#), [16](#)

- [65] Esther Rolf, Konstantin Klemmer, Caleb Robinson, and Hannah Kerner. Position: mission critical - satellite data is a distinct modality in machine learning. 2024. 1
- [66] Xian Shuai, Yiding Wang, Yimeng Wu, Xin Jiang, and Xiaozhe Ren. Scaling law for language models training considering batch size. *arXiv preprint arXiv:2412.01505*, 2024. 17
- [67] Michael J Smith, Luke Fleming, and James E Geach. EarthPT: a time series foundation model for earth observation. In *NeurIPS CCAI workshop*, 2023. 2
- [68] Caleb S Spradlin, Jordan A Caraballo-Vega, Jian Li, Mark L Carroll, Jie Gong, and Paul M Montesano. SatVision-TOA: A geospatial foundation model for coarse-resolution all-sky remote sensing imagery. *arXiv preprint arXiv:2411.17000*, 2024. 2
- [69] Jakub Straka and Ivan Gruber. Modernized training of u-net for aerial semantic segmentation. In *Proceedings of the IEEE/CVF Winter Conference on Applications of Computer Vision (WACV) Workshops*, pages 776–784, 2024. 8
- [70] Xian Sun, Peijin Wang, Wanxuan Lu, Zicong Zhu, Xiaonan Lu, Qibin He, Junxi Li, Xuee Rong, Zhujun Yang, Hao Chang, Qinfeng He, Guang Yang, Ruiping Wang, Jiwen Lu, and Kun Fu. RingMo a remote sensing foundation model with masked image modeling. *IEEE Transactions on Geoscience and Remote Sensing*, 61:1–22, 2023. 2
- [71] Daniela Szwarcman, Sujit Roy, Paolo Fraccaro, Þorsteinn Elí Gíslason, Benedikt Blumenstiel, Rinki Ghosal, Pedro Henrique de Oliveira, Joao Lucas de Sousa Almeida, Rocco Sedona, Yanghui Kang, et al. Prithvi-EO-2.0: A versatile multi-temporal foundation model for earth observation applications. *arXiv preprint arXiv:2412.02732*, 2024. 2
- [72] Maofeng Tang, Andrei Cozma, Konstantinos Georgiou, and Hairong Qi. Cross-Scale MAE: A tale of multiscale exploitation in remote sensing. *Advances in Neural Information Processing Systems*, 36:20054–20066, 2023. 2
- [73] Jiayuan Tian, Jie Lei, Jiaqing Zhang, Weiying Xie, and Yunsong Li. SwiMDiff: Scene-wide matching contrastive learning with diffusion constraint for remote sensing image. *IEEE Transactions on Geoscience and Remote Sensing*, 2024. 2
- [74] Jamie Tolan, Hung-I Yang, Benjamin Nosarzewski, Guillaume Couairon, Huy V Vo, John Brandt, Justine Spore, Sayantan Majumdar, Daniel Haziza, Janaki Vamaraju, et al. Very high resolution canopy height maps from rgb imagery using self-supervised vision transformer and convolutional decoder trained on aerial lidar. *Remote Sensing of Environment*, 300:113888, 2024. 5, 8, 19, 23
- [75] Zhan Tong, Yibing Song, Jue Wang, and Limin Wang. VideoMAE: Masked autoencoders are data-efficient learners for self-supervised video pre-training. *Advances in neural information processing systems*, 35:10078–10093, 2022. 6, 17
- [76] Hugo Touvron, Matthieu Cord, Matthijs Douze, Francisco Massa, Alexandre Sablayrolles, and Hervé Jégou. Training data-efficient image transformers & distillation through attention. In *International conference on machine learning*, pages 10347–10357. PMLR, 2021. 16
- [77] Gabriel Tseng, Ruben Cartuyvels, Ivan Zvonkov, Mirali Purohit, David Rolnick, and Hannah Kerner. Lightweight, pre-trained transformers for remote sensing timeseries. *arXiv preprint arXiv:2304.14065*, 2023. 2, 6, 18
- [78] Gabriel Tseng, Anthony Fuller, Marlena Reil, Henry Herzog, Patrick Beukema, Favyen Bastani, James R Green, Evan Shelhamer, Hannah Kerner, and David Rolnick. Galileo: Learning global & local features of many remote sensing modalities. In *Forty-second International Conference on Machine Learning*, 2025. 2, 6, 7, 18
- [79] Ashish Vaswani, Noam Shazeer, Niki Parmar, Jakob Uszkoreit, Llion Jones, Aidan N Gomez, Łukasz Kaiser, and Illia Polosukhin. Attention is all you need. *Advances in neural information processing systems*, 30, 2017. 16
- [80] Diego Velazquez, Pau Rodriguez, Sergio Alonso, Josep M Gonfaus, Jordi Gonzalez, Gerardo Richarte, Javier Marin, Yoshua Bengio, and Alexandre Lacoste. EarthView: A large scale remote sensing dataset for self-supervision. In *Proceedings of the Winter Conference on Applications of Computer Vision*, pages 1228–1237, 2025. 2, 3, 4, 18
- [81] Huy V Vo, Vasil Khalidov, Timothée Darcet, Théo Moutakanni, Nikita Smetanin, Marc Szafraniec, Hugo Touvron, Camille Couprie, Maxime Oquab, Armand Joulin, et al. Automatic data curation for self-supervised learning: A clustering-based approach. *arXiv preprint arXiv:2405.15613*, 2024. 8
- [82] Leonard Waldmann, Ando Shah, Yi Wang, Nils Lehmann, Adam Stewart, Zhitong Xiong, Xiao Xiang Zhu, Stefan Bauer, and John Chuang. Panopticon: Advancing any-sensor foundation models for earth observation. In *Proceedings of the Computer Vision and Pattern Recognition Conference*, pages 2204–2214, 2025. 2, 7
- [83] Di Wang, Qiming Zhang, Yufei Xu, Jing Zhang, Bo Du, Dacheng Tao, and Liangpei Zhang. Advancing plain vision transformer toward remote sensing foundation model. *IEEE Transactions on Geoscience and Remote Sensing*, 61:1–15, 2022. 2, 4
- [84] Di Wang, Jing Zhang, Minqiang Xu, Lin Liu, Dongsheng Wang, Erzong Gao, Chengxi Han, Haonan Guo, Bo Du, Dacheng Tao, et al. MTP: Advancing remote sensing foundation model via multi-task pretraining. *IEEE Journal of Selected Topics in Applied Earth Observations and Remote Sensing*, 2024.
- [85] Di Wang, Meiqi Hu, Yao Jin, Yuchun Miao, Jiaqi Yang, Yichu Xu, Xiaolei Qin, Jiaqi Ma, Lingyu Sun, Chenxing Li, Chuan Fu, Hongruixuan Chen, Chengxi Han, Naoto Yokoya, Jing Zhang, Minqiang Xu, Lin Liu, Lefei Zhang, Chen Wu, Bo Du, Dacheng Tao, and Liangpei Zhang. HyperSIGMA: Hyperspectral intelligence comprehension foundation model. *IEEE Transactions on Pattern Analysis and Machine Intelligence*, pages 1–18, 2025.
- [86] F Wang, H Wang, D Wang, Z Guo, Z Zhong, L Lan, J Zhang, Z Liu, and M Sun. Scaling efficient masked image modeling on large remote sensing dataset. *arXiv preprint arXiv:2406.11933*, 2024. 2
- [87] Fengxiang Wang, Hongzhen Wang, Yulin Wang, Di Wang, Mingshuo Chen, Haiyan Zhao, Yangang Sun, Shuo Wang,



- Long Lan, Wenjing Yang, et al. RoMA: Scaling up mamba-based foundation models for remote sensing. *arXiv preprint arXiv:2503.10392*, 2025. 2
- [88] Yi Wang, Conrad M Albrecht, and Xiao Xiang Zhu. Self-supervised vision transformers for joint sar-optical representation learning. In *IGARSS 2022-2022 IEEE International Geoscience and Remote Sensing Symposium*, pages 139–142. IEEE, 2022. 2
- [89] Yuelei Wang, Ting Zhang, Liangjin Zhao, Lin Hu, Zhechao Wang, Ziqing Niu, Peirui Cheng, Kaiqiang Chen, Xuan Zeng, Zhirui Wang, et al. RingMo-lite: A remote sensing multi-task lightweight network with cnn-transformer hybrid framework. *arXiv preprint arXiv:2309.09003*, 2023. 2
- [90] Yi Wang, Conrad M Albrecht, Nassim Ait Ali Braham, Chenying Liu, Zhitong Xiong, and Xiao Xiang Zhu. Decoupling common and unique representations for multi-modal self-supervised learning. In *European Conference on Computer Vision*, pages 286–303. Springer, 2024. 2
- [91] Yi Wang, Conrad M Albrecht, and Xiao Xiang Zhu. Multi-label guided soft contrastive learning for efficient earth observation pretraining. *IEEE Transactions on Geoscience and Remote Sensing*, 2024. 2
- [92] Yi Wang, Hugo Hernández Hernández, Conrad M Albrecht, and Xiao Xiang Zhu. Feature guided masked autoencoder for self-supervised learning in remote sensing. *IEEE Journal of Selected Topics in Applied Earth Observations and Remote Sensing*, 2024. 2
- [93] Yi Wang, Zhitong Xiong, Chenying Liu, Adam J Stewart, Thomas Dujardin, Nikolaos Ioannis Bountos, Angelos Zavvas, Franziska Gerken, Ioannis Papoutsis, Laura Leal-Taixé, et al. Towards a unified Copernicus foundation model for earth vision. *arXiv preprint arXiv:2503.11849*, 2025. 2
- [94] Xinye Wanyan, Sachith Seneviratne, Shuchang Shen, and Michael Kirley. Extending global-local view alignment for self-supervised learning with remote sensing imagery. In *Proceedings of the IEEE/CVF Conference on Computer Vision and Pattern Recognition*, pages 2443–2453, 2024. 2
- [95] Kang Wu, Yingying Zhang, Lixiang Ru, Bo Dang, Jiangwei Lao, Lei Yu, Luo Junwei, Zifan Zhu, Yue Sun, Jiahao Zhang, Qi Zhu, Jian Wang, Ming Yang, Jingdong Chen, and Yansheng Li. A semantic-enhanced multi-modal remote sensing foundation model for earth observation. *Nature Machine Intelligence*, pages 1–15, 2025. 2
- [96] Zhenda Xie, Zheng Zhang, Yue Cao, Yutong Lin, Jianmin Bao, Zhuliang Yao, Qi Dai, and Han Hu. SimMIM: a simple framework for masked image modeling. *2022 IEEE/CVF Conference on Computer Vision and Pattern Recognition (CVPR)*, pages 9643–9653, 2021. 1, 17
- [97] Zhitong Xiong, Yi Wang, Fahong Zhang, Adam J Stewart, Joëlle Hanna, Damian Borth, Ioannis Papoutsis, Bertrand Le Saux, Gustau Camps-Valls, and Xiao Xiang Zhu. Neural plasticity-inspired multimodal foundation model for earth observation. *arXiv preprint arXiv:2403.15356*, 2024. 2, 5, 8, 19, 23
- [98] Zongzhe Xu, Ritvik Gupta, Wenduo Cheng, Alexander Shen, Junhong Shen, Ameet Talwalkar, and Mikhail Khodak. Specialized foundation models struggle to beat supervised baselines. In *The Thirteenth International Conference on Learning Representations*, 2025. 7
- [99] Yang You, Jing Li, Sashank Reddi, Jonathan Hseu, Sanjiv Kumar, Srinadh Bhojanapalli, Xiaodan Song, James Demmel, Kurt Keutzer, and Cho-Jui Hsieh. Large batch optimization for deep learning: Training bert in 76 minutes. *arXiv preprint arXiv:1904.00962*, 2019. 17
- [100] Lixian Zhang, Yi Zhao, Runmin Dong, Jinxiao Zhang, Shuai Yuan, Shilei Cao, Mengxuan Chen, Juepeng Zheng, Weijia Li, Wei Liu, et al. A2-MAE: A spatial-temporal-spectral unified remote sensing pre-training method based on anchor-aware masked autoencoder. *arXiv preprint arXiv:2406.08079*, 2024. 2
- [101] Yingying Zhang, Lixiang Ru, Kang Wu, Lei Yu, Lei Liang, Yansheng Li, and Jingdong Chen. SkySense V2: A unified foundation model for multi-modal remote sensing. *arXiv preprint arXiv:2507.13812*, 2025. 2
- [102] Jinghao Zhou, Chen Wei, Huiyu Wang, Wei Shen, Cihang Xie, Alan Yuille, and Tao Kong. iBOT: Image BERT pre-training with online tokenizer. In *International Conference on Learning Representations*, 2022. 7

# MAESTRO: Masked AutoEncoders for Multimodal, Multitemporal, and Multispectral Earth Observation Data

## Supplementary Material

The appendix is structured as follows: Sec. 6 provides our full experimental details; Sec. 7 reports the detailed results for the experiments presented in Figs. 3 to 5 as well as additional ablation studies; Sec. 8 offers a qualitative analysis on inference results; Sec. 9 reports computational costs.

### 6. Experimental Details

In this section, we provide our full experimental details. We provide details on the four evaluated datasets (Sec. 6.1), details shared across models (Sec. 6.2), details specific to MAEs/MAESTRO (Sec. 6.3), and details specific to baseline FMs (Sec. 6.4). Additionally, we provide tables reporting the exhaustive list of hyperparameter values (Sec. 6.5).

#### 6.1. Experimental Details on the Datasets

In this subsection, we provide additional details on the choice of input modalities and labels for each of the four evaluated datasets (Secs. 6.1.1 to 6.1.4). We also report further details on the raw preprocessing steps applied to some input modalities of these datasets (Sec. 6.1.5).

##### 6.1.1. TreeSatAI-TS

TreeSat was introduced in [1], featuring aerial imagery (RGB + NIR) at 0.2 m resolution, together with monotemporal Sentinel-1 and Sentinel-2 data (Sentinel-2 provided as seasonal medians). It was later extended as TreeSatAI-TS in [4], adding Sentinel-1 and Sentinel-2 time series covering the full year closest to the aerial acquisition. In this work, we retain four distinct modalities: aerial imagery, Sentinel-1 time series in both orbits (ascending and descending), and Sentinel-2 time series. We disregard the original monotemporal Sentinel-1 and Sentinel-2 data.

The original labels introduced in [1] were formulated as regression targets, representing the spatial fraction of each tree species within a patch. Following [4, 5], we recast this as a multi-label classification task: a species class is considered present if its spatial fraction exceeds 0.07.

##### 6.1.2. PASTIS-HD

PASTIS was first introduced in [30] with Sentinel-2 time series spanning approximately one year. It was later extended as PASTIS-R in [31] by adding Sentinel-1 time series covering about 70 dates in both ascending and descending orbits, and further expanded in [4] as PASTIS-HD with SPOT 6–7 imagery resampled to 1 m resolution. We retain four distinct modalities: SPOT 6–7 imagery, Sentinel-1 time series in both orbits (ascending and descending), and Sentinel-2 time series.

The crop segmentation labels in [30] covered both semantic and panoptic segmentation. Here, we retain only the semantic segmentation labels, omitting panoptic segmentation. Restricting to semantic segmentation allows us to incorporate a spatialized fine-tuning task without introducing additional complexities related to specialized heads or loss functions. We assume that the spatialized nature of the task (e.g., semantic segmentation vs. classification) plays a more decisive role than the precise segmentation type (e.g., panoptic vs. semantic) when benchmarking different SSL approaches.

##### 6.1.3. FLAIR#2

FLAIR was introduced in [25] with 77,762 tiles of aerial and elevation imagery (RGB + NIR + DSM) at 0.2 m resolution. It was extended as FLAIR#2 in [26, 27] with Sentinel-2 time series spanning a full year in the form of superpatches, covering a larger spatial extent than the aerial imagery (400 m × 400 m vs. 102.4 m × 102.4 m) to provide additional spatial context. Following [5], we crop the Sentinel-2 time series to match the extent of the VHR imagery, discarding 93.5% of pixels. We also include elevation imagery at 0.2 m resolution, extracted from the FLAIR-HUB extension [28] on the 77,762 FLAIR#2 tiles. In total, we retain three distinct modalities: aerial imagery (RGB + NIR), elevation imagery (DEM + DSM), and Sentinel-2 time series.

We use the land cover semantic segmentation labels following the filtering procedure described in [25–27]: we retain only 12 of the 18 original classes, excluding the remaining 6 classes from the loss and metric computations.

### 6.1.4. FLAIR-HUB

FLAIR-HUB [28] is an extension of FLAIR#2 with 241,100 tiles of  $102.4 \text{ m} \times 102.4 \text{ m}$ . Compared to FLAIR#2, FLAIR-HUB enriches the elevation imagery (DEM + DSM) and treats it as a separate modality, crops the Sentinel-2 imagery to the extent of the aerial imagery (as we do in our version of FLAIR#2), and adds Sentinel-1 time series spanning a full year, as well as SPOT 6–7 imagery and historical aerial imagery. We retain five distinct modalities: aerial imagery (RGB + NIR), elevation imagery (DEM + DSM), Sentinel-1 time series in both orbits, and Sentinel-2 time series. We disregard the SPOT 6–7 imagery, which did not significantly improve fine-tuning performance—likely due to redundancy with the aerial modality—and the historical imagery, due to its lack of synchronicity with the labels.

We use the land cover semantic segmentation labels following the filtering procedure in [28]: we retain 15 of the 18 original classes, excluding the remaining 3 from the loss and metric computations. We omit the crop semantic segmentation labels.

### 6.1.5. Raw preprocessing

In TreeSatAI-TS, FLAIR#2, and FLAIR-HUB, the Sentinel-1 backscattering coefficient data is provided in linear scale. We apply a logarithmic transformation to express it in decibel (dB) scale (up to a multiplicative constant). For PASTIS-HD, the Sentinel-1 data is already in dB scale; however, we retain only the first two channels, corresponding to vertical (VV) and horizontal (VH) polarizations, and discard the third channel expressing their ratio (VV/VH).

In FLAIR#2 and FLAIR-HUB, we also apply a simple preprocessing step to the elevation imagery (DEM + DSM). We recast it as the DEM and a rescaled elevation defined as  $10^3 \times (\text{DSM} - \text{DEM})$ , ensuring that both channels have comparable value ranges.

The TreeSatAI-TS aerial imagery tiles have a slightly larger spatial extent than the other modalities ( $304 \times 304$  pixels, corresponding to 60.8 m, instead of  $300 \times 300$  pixels). We therefore apply a centered crop to align them spatially with the other inputs.

## 6.2. Experimental Details Shared across Models

In this subsection, we provide details on the preprocessing pipeline (Sec. 6.2.1), positional/temporal encodings (Sec. 6.2.2), data augmentation (Sec. 6.2.3), regularization (Sec. 6.2.4) and optimizers (Sec. 6.2.5).

### 6.2.1. Preprocessing

Here we provide the full details on the preprocessing pipeline introduced in Sec. 3.1. The full implementation is available in `ssl_models/dataset/dataset.py` in our code.

**Dataset-specific crop hyperparameter** Each dataset  $\mathcal{D}$  has a specific hyperparameter controlling the *spatial extent of crops* within original tiles. For classification tasks, where labels apply to entire tiles, we set the crop extent equal to the original tile extent. For segmentation tasks, the crop extent can be smaller, with the same crop applied to the segmentation labels. Choosing the crop size involves balancing two competing effects:

- Smaller crops increase the spatial resolution of the token grid under a fixed token budget. For a fixed token budget  $(I_m/P_m)^2 D_m$ , reducing the image size  $I_m$  reduces the patch size  $P_m$ , mitigating the risk of an information bottleneck in the tokenizer (the model’s entry block).
- Larger crops provide more spatial context for the model.

When cropping to a smaller extent than the original tile, we apply for each epoch a repetition factor  $R_{\mathcal{D}}$  equal to the ratio of the original tile area to the cropped area. This ensures that the total spatial area seen by the model in each epoch matches that of the full dataset. Practically, this means the dataset length is scaled by  $R_{\mathcal{D}}$ : each tile, originally mapped to a single index, is now associated with  $R_{\mathcal{D}}$  indices, effectively repeating it that many times with different crops.

The *crop sampling* strategy differs between training and validation/testing:

- *Training*: the crop is sampled randomly from all valid crops within the tile, subject only to the constraint that crop boundaries align with integer pixel indices for each modality  $m$ .
- *Validation and testing*: tiles are partitioned into non-overlapping crops, which are iterated over exhaustively. The same repetition factor is applied in the test epoch, ensuring test metrics cover the exact same spatial footprint as the original tiles.

In practice, we use the full tile extent for TreeSatAI-TS, FLAIR#2, and FLAIR-HUB. For PASTIS-HD, however, we found it beneficial to substantially reduce the crop size. This allows us to set  $P_m = 2$  with  $D_m = 16$  and  $D_m = 4$  temporal bins for Sentinel-2 and Sentinel-1, respectively. Without cropping, keeping the same token budget and number of temporal bins would have required  $P_m = 16$  for these modalities.

**Modality-specific hyperparameters.** Each modality  $m$  in the dataset  $\mathcal{D}$  has a configurable set of preprocessing hyperparameters:

- The *image size*  $I_m$ , which by default corresponds to the number of pixels covering the spatial extent of the crop (however, this can be adjusted for baseline FMs to match a specific transferred patch size  $P_m$ );
- The *target number of temporal bins*  $D_m$ ;
- Whether a *snow/cloud mask* is used to guide valid time step selection within temporal bins, and the *probability threshold* for disregarding mask values above this threshold;
- A *constant multiplicative normalization factor* applied to the modality.

**Preprocessing steps.** The `__getitem__` method of our datasets operates in three steps:

- Determine the sampled dataset tile based on the dataset index;
- Sample a spatial crop shared across all modalities  $m \in \mathcal{D}$ ;
- Process each modality  $m$  based on the sampled crop.

Processing step (iii) for each modality  $m$  proceeds as follows:

- If the number of original time steps  $T_m$  is not a multiple of  $D_m$ , randomly truncate the sequence to  $D_m \times \lceil T_m/D_m \rceil$  consecutive time steps.
- Read the corresponding tile section defined by the crop’s spatial extent and the (potentially truncated) temporal extent. To minimize I/O overhead, we use lazy loading:
  - For `.tif` files: read with `rasterio` using window reading.
  - For `.npy` files: read with `numpy.load` using the argument `mmap_mode="r"`.
  - For `.h5` files: read with `h5py.File` in read mode, and index the required array sections.
- Reshape the array into  $D_m$  temporal bins.
- For each temporal bin, sample one time step inside the bin:
  - If a snow/cloud mask is used, filter out time steps that include any mask values above the configured threshold. An exception occurs when no valid time steps remain, in which case all time steps in the bin are retained.
  - Select a single time step from the remaining ones. During training, the selection is random to serve as data augmentation. During validation and testing, we maximize representativeness by: computing the pixel-wise median across valid time steps in the temporal bin; computing the mean absolute deviation to this median for each time step; and selecting the time step with the lowest mean absolute deviation.
- If the image size  $I_m$  does not match the number of pixels covering the spatial extent of the crop, interpolate the array spatially with `torch.nn.functional.interpolate` using `mode="nearest"`.
- Scale the array by the configured constant normalization factor.

### 6.2.2. Positional/Temporal Encodings

As noted in Sec. 3.1, we do not include explicit modality encodings, since we use modality-specific tokenizers and learnable modality-specific [mask] tokens that implicitly encode the source or target modality for each token. However, we do include spatial and temporal positional encodings, as detailed below.

**Spatial encodings.** To encode spatial information, we follow the common practice of using two-dimensional sine–cosine positional encodings [34, 76, 79]. As in Scale-MAE [64], we scale these positional encodings according to the ground sampling distance of each modality. Concretely, we compute the *least common multiple* (LCM) of the token grid sizes across modalities, i.e.,  $\text{lcm}_{m \in \mathcal{D}} \{I_m/P_m\}$ , and generate positional encodings on the high-resolution grid defined by this LCM. For each modality  $m$ , we then obtain its positional encodings by downsampling the high-resolution grid, averaging over all high-resolution grid cells corresponding to each low-resolution grid cell.

**Temporal encodings.** To encode temporal information, we first extract the day of year and hour of day for the selected time step in each temporal bin (see Sec. 6.2.1). The day of year is normalized by 365.25 and the hour of day by 24. Applying sine and cosine transformations to these normalized values yields four temporal features per time step.

In addition, for each tile, we define a reference date shared across all modalities  $m$  to capture temporal differences across years, rather than only within a single year (as we would be limited to with just sine/cosine encodings). For each time step, we compute the difference between its acquisition date and this reference date, obtaining a fifth temporal feature. This value is then duplicated four times, resulting in a total of eight temporal features per time step.

**Aggregation.** Spatial and temporal encodings are aggregated by concatenation. In the encoder with latent dimension  $C_e$ , the spatial encodings occupy  $C_e - 8$  dimensions, while the temporal encodings use 8 dimensions, leading to  $C_e$  dimensions after concatenation. The same approach is applied in the decoder with latent dimension  $C_d$ .



### 6.2.3. Data Augmentation

We use up to three types of data augmentation:

- *Random spatial cropping*: During training, a crop of the configured extent is randomly sampled within the original tile at the start of preprocessing. This is disabled for validation and testing, where tiles are instead partitioned into non-overlapping crops processed exhaustively in each epoch. When the crop extent matches the original tile extent, this augmentation is implicitly disabled, even during training.
- *Random time step selection*: During training, time steps are randomly sampled from the valid steps within each temporal bin. For validation and testing, we instead select time steps that maximize representativeness among valid steps.
- *D4 augmentation*: Throughout training, validation, and testing, synchronized D4 transformations are applied across all modalities and semantic segmentation labels just after the preprocessing pipeline. We retain this augmentation for validation and testing, as the model is assumed to have learned equivariance to these transformations during training.

### 6.2.4. Regularization

As regularization, we apply an Exponential Moving Average (EMA) of the model weights during fine-tuning [56], similar to Stochastic Weight Averaging [38]. Concretely, an EMA of the weights is updated at each epoch with a smoothing window equal to 20% of the total fine-tuning epochs. Denoting the model weights by  $\theta$  and their EMA by  $\theta_{\text{EMA}}$ , the EMA weights are initialized as  $\theta$  and updated at each epoch as:

$$\theta_{\text{EMA}} = \alpha \theta_{\text{EMA}} + (1 - \alpha) \theta, \quad \alpha = 1 - (0.2 \times N_{\text{epochs}})^{-1}.$$

During validation and testing, we use the EMA weights instead of the regular model weights.

### 6.2.5. Optimizer

In all experiments, we use the AdamW optimizer [51]. The learning rate is scaled with the square root of the batch size [44, 53, 66, 99]; that is, we set the learning rate equal to the base learning rate multiplied by the square root of the batch size. However, for a given dataset and training phase (i.e., SSL pre-training, probing, or fine-tuning), we keep the batch size and learning rate fixed across experiments to avoid any confounding factors.

Across all phases—SSL pre-training, probing, and fine-tuning—we use a cosine decay learning rate scheduler with a single cycle and a warm-up period. This approach is common in recent SSL studies with Transformers in computer vision [10, 34, 60, 96]. We implement this using `torch.optim.lr_scheduler.OneCycleLR` with its default annealing strategy and a warm-up for 20% of the total epochs.

During SSL pre-training and probing, the learning rate is annealed down to  $1 \times 10^{-4}$  times its maximum value. During fine-tuning, it is instead annealed only to half of the maximum learning rate. This helps fully leverage the EMA strategy as weight averaging (i) naturally reduces noise [56] and (ii) benefits from greater model diversity along the training trajectory when the learning rate remains sufficiently high.

## 6.3. Experimental Details Specific to MAEs/MAESTRO

In this subsection, we provide experimental details specific to MAEs/MAESTRO. We detail the masking strategy (Sec. 6.3.1) and the selection of band groups for patch-group-wise normalization (Sec. 6.3.2).

### 6.3.1. Masking Strategy

We adopt a masking strategy that proceeds in two stages:

(i) **Structured Masking:**

- (a) *Modality structure*: Mask each modality with a fixed probability of 0.25;
- (b) *Spatial structure*: Within each modality, mask each spatial position with a fixed probability of 0.25;
- (c) *Temporal structure*: Within each modality, mask each temporal position with a fixed probability of 0.25.

(ii) **Unstructured Masking:** Adjust the masking from step (i) to match an overall 75% masking ratio:

- (a) If step (i) results in too few masked tokens, randomly mask additional unmasked tokens;
- (b) If step (i) results in too many masked tokens, randomly unmask some of them.

Our masking strategy relates to several approaches proposed in previous works, as outlined below:

- Step (i-a), which introduces modality-structured masking, is conceptually similar to the band-masking strategy in FomoNet [9], although a direct equivalence would require treating each spectral band as a distinct modality.
- Step (i-b), which introduces spatially-structured masking, aligns with the consistent masking used in SatMAE [13] and the tube masking in VideoMAE [75]. It also resembles the approach in SeaMo [46], but with a key distinction: SeaMo

enforces consistency across modalities at a single time step, whereas we enforce consistency across time steps within a single modality.

- Step (i-c), which introduces temporally-structured masking, corresponds to the “Timesteps” strategy in Presto [77].
- Our combined masking strategy shares similarities with those in AnySat [5], EarthMAE [80], and Galileo [78], but still differs in important ways. AnySat and Galileo apply only spatially- and temporally-structured masking, while EarthMAE uses only spatially-structured masking. Moreover, the way in which we integrate the structured and unstructured stages is distinct from these methods.

### 6.3.2. Band Groups

Here, we provide details on our selection of spectral band groups for patch-group-wise normalization.

We start by computing per-band histograms for the VHR, Sentinel-1, and Sentinel-2 modalities on TreeSatAI-TS, PASTIS-HD, and FLAIR-HUB. To reduce computational cost, a toy version of FLAIR-HUB containing 250 tiles was used for histogram computation. The resulting histograms are shown in Fig. 6a, Fig. 6b, and Fig. 6c.

For VHR aerial imagery, the RED, GREEN, and BLUE bands exhibit relatively similar histograms, whereas the NIR band shows a distinct distribution.

For Sentinel-1, the histograms of VV and VH differ markedly, in line with their differing polarization responses; VH generally exhibits lower backscatter than VV.

For Sentinel-2, the ten bands cluster into three natural groups with strong intra-group similarity but higher inter-group variation.

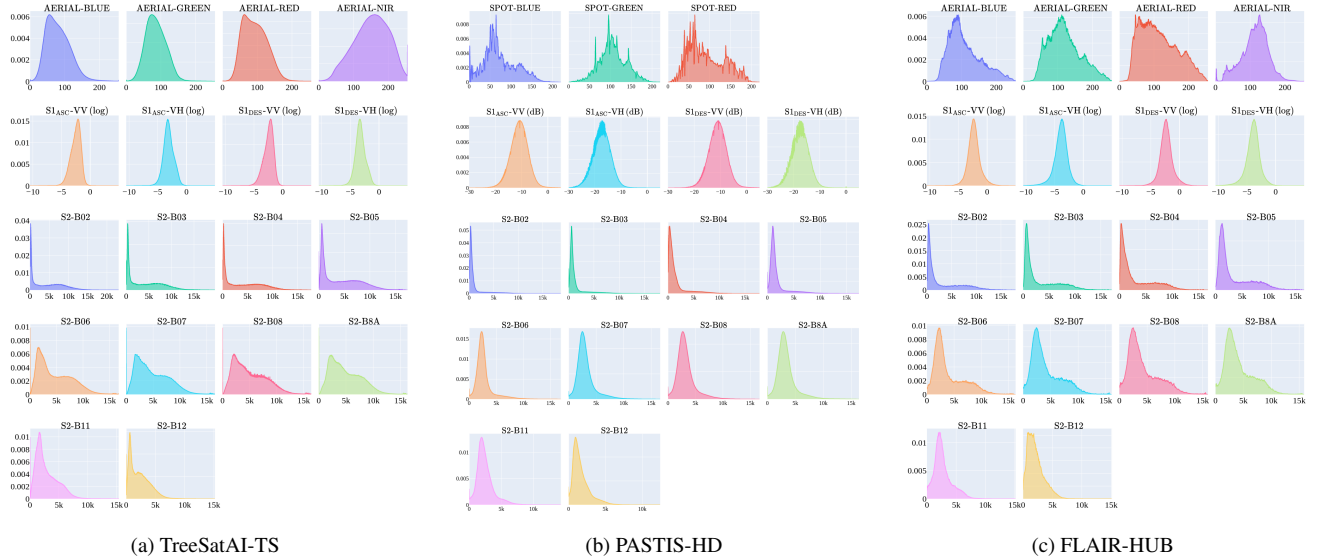


Figure 6. Per-band histograms for VHR, Sentinel-1, and Sentinel-2 modalities on the TreeSatAI-TS, PASTIS-HD, and FLAIR-HUB datasets.

Based on these insights, we define the spectral band groups detailed in Tab. 2 for patch-group-wise normalization.

Table 2. Spectral band groups selected for patch-group-wise normalization.

Modality	Group 1	Group 2	Group 3
Aerial	RED, GREEN, BLUE	NIR	
SPOT	RED, GREEN, BLUE		
$S1_{ASC} / S1_{DES}$	VV	VH	
S2	B02, B03, B04, B05	B06, B07, B08, B8A	B11, B12

Note that the Sentinel-2 band groups follow the natural wavelength order, which does not precisely align with the order of spatial resolutions (e.g., band B05 has 20 m resolution, while B08 has 10 m). This contrasts with some prior approaches to S2 band grouping [13, 37].

## 6.4. Experimental Details Specific to Baseline FMs

In this subsection, we describe the FMs used as baselines in our comparative evaluation of MAESTRO, along with their specific adaptations to our context. The selected models include DINO-v2 sat. [74], CROMA [24], and DOFA [97], which are pre-trained on EO data, as well as DINO-v2 [60], which is pre-trained on natural images.

To optimize the performance of these baseline FMs in our experimental setup, we introduce several key adaptations:

- (i) **Input resizing:** Images are resized to match MAESTRO’s token grid while preserving the original patch size (see Tabs. 5 to 7).
- (ii) **Multimodal tokenization:** Multiple modalities are processed simultaneously via parallel, modality-specific tokenizers. For DINO-v2 and DINO-v2 sat., tokenizers are adapted to transfer RGB weights while still allowing the handling of non-RGB inputs.
- (iii) **Late fusion:** For DINO-v2, DINO-v2 sat., and DOFA, we incorporate late fusion across modalities and time steps using the *shared* and *monotemp* fusion modes (see Sec. 3.1). For CROMA, specific multimodal and multitemporal fusion modes are used.
- (iv) **Temporal encoding:** As these baseline FMs lack native temporal handling, temporal encodings from Sec. 6.2.2 are injected into embedded tokens *after* the encoder. This choice avoids disrupting the transferred representations.

All baseline FMs natively use ViT backbones [19], as in MAESTRO. We also use the same classification and segmentation heads as in MAESTRO.

Details on the pre-training modalities and the modalities selected for fine-tuning are provided in Tab. 3.

Table 3. Pre-training modalities and modalities selected for fine-tuning for the different baseline FMs.

Model	Pre-training modalities	Fine-tuning modalities			
		VHR	S1 <sub>ASC</sub> /S1 <sub>DES</sub>	S2	DEM/DSM
DINO-v2 [60]	Natural RGB images (LVD-142M dataset)	✓	✗	✓	✗
DINO-v2 sat. [74]	Maxar Vivid2 mosaic imagery	✓	✗	✓	✗
DOFA [97]	Sentinel-1, Sentinel-2, Gaofen, NAIP, EnMaP	✓	✓	✓	✗
CROMA [24]	Sentinel-1, Sentinel-2 (SSL4EO dataset)	✗	✓	✓	✗

### 6.4.1. DINO-v2 and DINO-v2 sat.

DINO-v2 [60] is a FM pre-trained on natural RGB images using a SSL teacher–student distillation framework, which combines global (image-level) and local (patch-level) objectives. Due to the domain gap between natural and EO imagery, transferring DINO-v2 to EO tasks is non-trivial.

To adapt it to our multimodal setting, we modify its patchification operation to support both VHR and Sentinel-2 inputs using two parallel patchification layers. For PASTIS-HD, FLAIR#2, and FLAIR-HUB, we retain the pre-trained RGB channel weights, while additional channels are initialized with near-zero values to minimize disruption, following [23]. In contrast, for TreeSatAI-TS, we found it beneficial to map the pre-trained RGB weights to the infrared colors (IRC) channels NIR, RED, and GREEN in the downstream task, while initializing the BLUE channel weights with near-zero values. We attribute this beneficial effect to two factors: (i) representations learned on natural RGB images transfer well to IRC aerial imagery, and (ii) the NIR channel plays a decisive role in TreeSatAI-TS, benefiting from being mapped to the transferred weights.

We experiment with two fusion modes for handling multimodality and multitemporality: (i) *shared*, where a single encoder (initialized from DINO-v2’s weights) processes all modalities and time steps independently, with shared weights across them, (ii) *monotemp*, where modality-specific encoders (also initialized from DINO-v2) process each modality and time step independently. Since DINO-v2 lacks native temporal handling, the temporal encodings of Sec. 6.2.2 are injected into the post-encoder token embeddings. The class token is discarded.

DINO-v2 sat. [74] is based on the same architecture as DINO-v2 but pre-trained on Maxar’s very high-resolution RGB satellite imagery. We apply the same adaptation protocol for this model as for DINO-v2.

### 6.4.2. DOFA

DOFA [97] is a FM pre-trained on multi-source EO data using the MAE framework and a dynamic channel handling via a hypernetwork that generates patch embedding weights based on input wavelengths (see Table 4). While DOFA is inherently flexible, adaptations are required to support multimodality and multitemporality in our context.

We implement four parallel patchification layers (initialized from the original patchification layer) to handle VHR, Sentinel-2, and Sentinel-1 in both ascending and descending orbits. As with DINO-v2 and DINO-v2 sat., we explore both

*shared* and *monotemp* fusion modes for handling multimodality and multitemporality. Since the original model lacks native temporal handling, the temporal encodings of Sec. 6.2.2 are again injected into the post-encoder token embeddings.

Table 4. **DOFA’s wavelengths per modality.**

Modality	Bands	Wavelengths
Aerial	RED, GREEN, BLUE, NIR	0.64, 0.56, 0.48, 0.81
SPOT	RED, GREEN, BLUE	0.66, 0.56, 0.48
S1 <sub>ASC</sub>	VV, VH	5.405, 5.405
S1 <sub>DES</sub>	VV, VH	5.405, 5.405
S2	B02, B03, B04, B05, B06, B07, B08, B8A, B11, B12	0.490, 0.560, 0.665, 0.705, 0.740, 0.783, 0.842, 0.865, 1.610, 2.190

### 6.4.3. CROMA

CROMA [24] is a FM specifically designed for Sentinel imagery, featuring separate encoders for Sentinel-1 and Sentinel-2, coupled via a cross-encoder that fuses their intermediate representations. Since we fine-tune CROMA only on its original modalities, only minimal adaptations are required. The time series for Sentinel-1 in ascending and descending orbits are concatenated and passed as a single sequence to the Sentinel-1 encoder. As with other baseline FMs, temporal encodings are injected post-encoder.

We consider two fusion modes for handling multimodality and multitemporality: (i) *late-croma*, where monotemporal Sentinel-1 and Sentinel-2 encoder outputs are concatenated across modalities and time steps before the classification/segmentation heads (cross-encoder disabled); (ii) *inter-croma* (default), where monotemporal Sentinel-1 and Sentinel-2 encoder outputs are grouped into pairs, fused via the cross-encoder, and finally concatenated across pairs before the classification/segmentation heads.

Note that CROMA remains intrinsically monotemporal: *late-croma* performs only late multitemporal fusion, while *inter-croma* performs intermediate multitemporal fusion within individual Sentinel-1/Sentinel-2 pairs, but late fusion across pairs.

## 6.5. Hyperparameter Tables

In this subsection, we provide tables reporting the exhaustive list of our hyperparameter values.

### 6.5.1. Dataset-specific Hyperparameters

Table 5. **TreeSatAI-TS’s hyperparameters.**

	Spatial extent of original tiles: 60 m Spatial extent of crops: 60 m			
	Aerial	S1 <sub>ASC</sub>	S1 <sub>DES</sub>	S2
Dataset’s original resolution (m)	0.2	10	10	10
Image size ( $I_m$ )				
MAE/MAESTRO/ViT	300	6	6	6
DINO-v2	210	✗	✗	42
DINO-v2 sat.	240	✗	✗	48
DOFA	240	48	48	48
CROMA	✗	24	24	24
Patch size ( $P_m$ )				
MAE/MAESTRO/ViT	20	2	2	2
DINO-v2	14	✗	✗	14
DINO-v2 sat.	16	✗	✗	16
DOFA	16	16	16	16
CROMA	✗	8	8	8
Number of temporal bins ( $D_m$ )	1	4	4	16
Number of channels ( $C_m$ )	4	2	2	10
Multiplicative normalization factor	255	5	5	$5 \times 10^3$
Use cloud/snow mask				✓(mask proba. > 0)
MAE/MAESTRO’s band groups ( $\mathcal{G}_m$ )	RED, GREEN, BLUE NIR	VV VH	VV VH	B02, B03, B04, B05 B06, B07, B08, B8A B11, B12



Table 6. PASTIS-HD’s hyperparameters.

Spatial extent of original tiles: 1280 m Spatial extent of crops: 160 m Spatial resolution of token grid of reference: 20 m				
	SPOT	S1 <sub>ASC</sub>	S1 <sub>DES</sub>	S2
Dataset’s orig. resolution (m)	1	10	10	10
Image size ( $I_m$ )				
MAE/MAESTRO/ViT	160	16	16	16
DINO-v2	140	✗	✗	112
DINO-v2 sat.	160	✗	✗	128
DOFA	160	128	128	128
CROMA	✗	64	64	64
Patch size ( $P_m$ )				
MAE/MAESTRO/ViT	16	2	2	2
DINO-v2	14	✗	✗	14
DINO-v2 sat.	16	✗	✗	16
DOFA	16	16	16	16
CROMA	✗	8	8	8
Number of temporal bins ( $D_m$ )	1	4	4	16
Number of channels ( $C_m$ )	3	2	2	10
Multiplicative normalization factor	255	20	20	$1 \times 10^4$
Use cloud/snow mask				✗ (not avail.)
MAE/MAESTRO’s band groups ( $\mathcal{G}_m$ )	RED, GREEN, BLUE	VV VH	VV VH	B02, B03, B04, B05 B06, B07, B08, B8A B11, B12

Table 7. FLAIR#2’s and FLAIR-HUB’s hyperparameters.

Spatial extent of original tiles: 102.4 m Spatial extent of crops: 102.4 m Spatial resolution of token grid of reference: 3.2 m					
	Aerial	DEM/DSM	S1 <sub>ASC</sub>	S1 <sub>DES</sub>	S2
Present in FLAIR#2	✓	✓	✗	✗	✓
Dataset’s original resolution (m)	0.2	0.2	10.24	10.24	10.24
Image size ( $I_m$ )					
MAE/MAESTRO/ViT	512	512	10	10	10
DINO-v2	448	✗	✗	✗	70
DINO-v2 sat.	512	✗	✗	✗	80
DOFA	512	✗	80	80	80
CROMA	✗	✗	40	40	40
Patch size ( $P_m$ )					
MAE/MAESTRO/ViT	16	32	2	2	2
DINO-v2	14	✗	✗	✗	14
DINO-v2 sat.	16	✗	✗	✗	16
DOFA	16	✗	16	16	16
CROMA	✗	✗	8	8	8
Number of temporal bins ( $D_m$ )	1	1	4	4	16
Number of channels ( $C_m$ )	4	2	2	2	10
Multiplicative normalization factor	255	$1 \times 10^3$	5	5	$5 \times 10^3$
Use cloud/snow mask					✓(mask proba. > 0)
MAE/MAESTRO’s band groups ( $\mathcal{G}_m$ )	RED, GREEN, BLUE NIR	DEM, DSM	VV VH	VV VH	B02, B03, B04, B05 B06, B07, B08, B8A B11, B12

### 6.5.2. Data Augmentation/Regularization Hyperparameters

Table 8. Data augmentation/regularization hyperparameters.

Augmentation/Regularization	Phase used	Hyperparameter
Random spatial cropping	Pre-train/Probe/Fine-tune	
Random time step selection	Pre-train/Probe/Fine-tune	
D4 augmentation	Pre-train/Probe/Fine-tune	
EMA [56]	Fine-tune	$\alpha = 1 - (0.2 \times N_{\text{epochs}})^{-1}$

### 6.5.3. Optimizer Hyperparameters

Table 9. Optimizer hyperparameters.

Phase	Hyperparameter	TreeSatAI-TS	PASTIS-HD	FLAIR#2	FLAIR-HUB
	Optimizer	AdamW	AdamW	AdamW	AdamW
	LR schedule	cosine decay	cosine decay	cosine decay	cosine decay
	Warmup fraction	20%	20%	20%	20%
	Weight decay	$1 \times 10^{-2}$	$1 \times 10^{-2}$	$1 \times 10^{-2}$	$1 \times 10^{-2}$
	$\beta_1$	0.9	0.9	0.9	0.9
	$\beta_2$	0.99	0.99	0.99	0.99
Pre-train	Base learning rate	$3 \times 10^{-5}$	$3 \times 10^{-5}$	$3 \times 10^{-5}$	$3 \times 10^{-5}$
	Final div. factor	$1 \times 10^4$	$1 \times 10^4$	$1 \times 10^4$	$1 \times 10^4$
	Batch size				
	Dataset frac. 100%	96	72	72	144
	Dataset frac. 20%	96	72	–	72
	Dataset frac. 5%	96	72	–	72
	Epochs				
	Dataset frac. 100%	100	100	100	100
	Dataset frac. 20%	200	200	–	100
	Dataset frac. 5%	400	400	–	200
Probe	Base learning rate	$1 \times 10^{-5}$	$1 \times 10^{-5}$	$1 \times 10^{-5}$	$1 \times 10^{-5}$
	Final div. factor	$1 \times 10^4$	$1 \times 10^4$	$1 \times 10^4$	$1 \times 10^4$
	Batch size				
	Dataset frac. 100%	96	48	48	96
	Dataset frac. 20%	96	48	–	48
	Dataset frac. 5%	96	48	–	48
	Epochs				
	Dataset frac. 100%	10	10	15	15
	Dataset frac. 20%	20	20	–	15
	Dataset frac. 5%	40	40	–	30
Fine-tune	Base learning rate	$1 \times 10^{-5}$	$1 \times 10^{-5}$	$1 \times 10^{-5}$	$1 \times 10^{-5}$
	Final div. factor	2	2	2	2
	Batch size				
	Dataset frac. 100%	96	48	48	96
	Dataset frac. 20%	96	48	–	48
	Dataset frac. 5%	96	48	–	48
	Epochs				
	Dataset frac. 100%	50	50	100	100
	Dataset frac. 20%	100	100	–	100
	Dataset frac. 5%	200	200	–	200

#### 6.5.4. SSL Hyperparameters

Table 10. SSL hyperparameters.

Hyperparameter	
Reconstruction loss	$L_1$ w/ patch-group-wise normalization (for some ablations: $L_1$ w/o normalization or $L_1$ w/ patch-wise normalization)
Masking ratio	75%
Probability modality-structured masking	0.25 (if not disabled)
Probability temporally-structured masking	0.25 (if not disabled)
Probability spatially-structured masking	0.25 (if not disabled)

## 7. Additional Results

In this section, we report the detailed results on multimodal and multitemporal fusion (Sec. 7.1), multispectral fusion and target normalization (Sec. 7.2), and scaling with respect to pre-training and fine-tuning dataset size (Sec. 7.3). We also report additional ablations on our masking strategy (Sec. 7.4), the impact of multitemporal components (Sec. 7.5), and the importance of each modality by dataset (Sec. 7.6).

### 7.1. Multimodal/Multitemporal Fusion

The detailed numbers of the evaluation of the different multimodal and multitemporal fusion modes with MAEs, baseline FMs and ViTs can be found in Tab. 11, in addition to Fig. 3.

Table 11. **Evaluation of different multimodal and multitemporal fusion modes for MAEs, baseline FMs and ViTs across three datasets.** We report the weighted F1 score (%) on TreeSatAI-TS and the mIoU (%) on PASTIS-HD and FLAIR-HUB 20%.

Model	Model size	Fusion mode	Modality groups	TreeSatAI-TS	PASTIS-HD fold I	FLAIR-HUB filt. 20% / split 1
MAE	Base	shared		76.1	66.1	62.5
MAE	Base	monotemp		77.0	66.0	62.4
MAE	Base	mod		78.4	68.9	63.3
MAE	Base	group	$S1_{ASC}, S1_{DES}$	78.5	68.8	<b>63.6</b>
MAE	Base	group	$S1_{ASC}, S1_{DES}, S2$	78.1	<b>69.1</b>	63.5
MAE	Base	group	$S1_{ASC}, S1_{DES}, S2, VHR$	78.2	68.1	61.4
MAE	Base	inter-group	$S1_{ASC}, S1_{DES}$	<b>78.8</b>	68.6	63.5
DINO-v2 [60]	Base	shared		<b>76.7</b>	64.4	64.2
DINO-v2 [60]	Base	monotemp		76.4	63.7	63.9
DINO-v2 sat. [74]	Large	shared		76.3	64.0	<b>64.5</b>
DINO-v2 sat. [74]	Large	monotemp		76.6	63.1	64.0
DOFA [97]	Base	shared		76.1	62.9	62.8
DOFA [97]	Base	monotemp		75.9	63.2	64.1
CROMA [24]	Base	late-croma		69.8	64.9	41.9
CROMA [24]	Base	inter-croma		70.5	<b>65.0</b>	42.5
ViT	Base	shared		72.6	64.1	59.3
ViT	Base	monotemp		73.0	64.4	58.9
ViT	Base	mod		75.4	<b>64.6</b>	59.0
ViT	Base	group	$S1_{ASC}, S1_{DES}$	75.7	64.6	<b>59.5</b>
ViT	Base	group	$S1_{ASC}, S1_{DES}, S2$	<b>76.0</b>	64.2	59.1
ViT	Base	group	$S1_{ASC}, S1_{DES}, S2, VHR$	75.9	64.0	56.4
ViT	Base	inter-group	$S1_{ASC}, S1_{DES}$	75.6	64.5	58.8

### 7.2. Multispectral Fusion/Target Normalization

The detailed numbers of the evaluation of the different choices of multispectral fusion and target normalization with MAEs can be found in Tab. 12, in addition to Fig. 4. We also report results after probing evaluation in Tab. 13.

We observe a slight performance drop when using token-based fusion with patch-wise normalization compared to joint-token fusion with patch-group-wise normalization. This may be attributed to the combination of two factors: (i) certain

Sentinel-2 band groups may be less relevant to the downstream tasks, and (ii) our segmentation heads, which aggregate multimodal and multitemporal features through a single attentive pooling layer, are shallow and may struggle to filter out irrelevant tokens—thereby introducing noise into the final predictions.

Table 12. **Evaluation of different choices of multispectral fusion and target normalization for MAE-B models across two datasets.** We report the weighted F1 score (%) on TreeSatAI-TS and the mIoU (%) on PASTIS-HD, with varying pre-training dataset fractions.

Multispectral fusion	Target normalization	TreeSatAI-TS			PASTIS-HD fold I		
		Pre-training dataset frac.			Pre-training dataset frac.		
		5%	20%	100%	5%	20%	100%
Joint-token	No normalization	72.7	72.8	74.6	64.9	65.4	65.1
Joint-token	Patch-wise	74.4	75.5	77.4	66.7	67.1	67.5
Joint-token	Patch-group-wise	<b>76.3</b>	<b>77.4</b>	<b>78.5</b>	<b>67.3</b>	<b>68.1</b>	<b>68.8</b>
Token-based	Patch-wise	<b>76.6</b>	<b>77.0</b>	<b>78.9</b>	<b>66.7</b>	<b>67.2</b>	<b>68.6</b>

Table 13. **Probing evaluation of different choices of multispectral fusion and target normalization for MAE-B models across two datasets.** We report the weighted F1 score (%) on TreeSatAI-TS and the mIoU (%) on PASTIS-HD, with varying pre-training dataset fractions.

Multispectral fusion	Target normalization	TreeSatAI-TS			PASTIS-HD fold I		
		Pre-training dataset frac.			Pre-training dataset frac.		
		5%	20%	100%	5%	20%	100%
Joint-token	No normalization	57.2	61.1	63.2	52.5	56.9	57.9
Joint-token	Patch-wise	62.9	65.1	67.7	58.2	59.7	61.2
Joint-token	Patch-group-wise	<b>64.8</b>	<b>68.6</b>	<b>69.3</b>	<b>59.0</b>	<b>60.2</b>	<b>61.2</b>
Token-based	Patch-wise	<b>61.9</b>	<b>66.2</b>	<b>69.3</b>	<b>55.9</b>	<b>57.5</b>	<b>61.0</b>

### 7.3. Scaling by Dataset Size

The detailed numbers of the performance with different pre-training/fine-tuning dataset fractions are provided in Tab. 14, in addition to Fig. 5.

Across all settings, SSL pre-training with MAESTRO outperforms supervised ViTs, with particularly large gains when fine-tuning data is scarce. Comparing “Pre-training fraction = 100%” and “Pre-training fraction = Fine-tuning fraction” in the table highlights that additional pre-training data improves downstream performance regardless of the amount of labeled data available for fine-tuning. This suggests that MAESTRO could further benefit from larger-scale unlabeled pre-training.

Table 14. **Scaling of MAESTRO-B and ViT-B models with different pre-training/fine-tuning dataset fractions across three datasets.** We report the weighted F1 score (%) on TreeSatAI-TS and the mIoU (%) on PASTIS-HD and FLAIR-HUB for three fine-tuning dataset fractions: 5%, 20%, and 100%. For each fine-tuning fraction, we compare three pre-training settings: no pre-training, pre-training on the same fraction as fine-tuning, and pre-training on 100% of the data. Note that when fine-tuning on 100% of the data, pre-training on the same fraction as fine-tuning and pre-training on 100% of the data become equivalent, hence the identical performance.

	TreeSatAI-TS			PASTIS-HD fold I			FLAIR-HUB split 1		
	Fine-tuning dataset frac.			Fine-tuning dataset frac.			Fine-tuning dataset frac.		
	5%	20%	100%	5%	20%	100%	5%	20%	100%
No pre-training	61.8	69.0	75.7	38.8	52.2	64.6	55.3	59.5	61.6
Pre-training fraction = Fine-tuning fraction	65.5	71.8	78.5	46.6	57.1	68.8	60.1	63.6	64.9
Pre-training fraction = 100%	<b>67.8</b>	<b>73.8</b>	<b>78.5</b>	<b>52.5</b>	<b>59.2</b>	<b>68.8</b>	<b>61.5</b>	<b>64.6</b>	<b>64.9</b>



## 7.4. Masking Strategy

We examine the impact of various components of our masking strategy on downstream task performance. In particular, we assess the effect of including the different structured masking steps—namely steps (i-a), (i-b), and (i-c) detailed in Sec. 6.3.1—in the SSL pretext task. Results are reported in Tab. 16 and Tab. 15, corresponding to performance after fine-tuning and probing, respectively. In these experiments, we use the *group* fusion mode, grouping together the Sentinel-1 ascending and descending modalities. For multispectral data, we use *joint-token* fusion combined with *patch-group-wise* target normalization during reconstruction.

We find that structured masking yields only marginal improvements in fine-tuning performance. However, temporally structured masking leads to a notable boost in probing performance on PASTIS-HD. This suggests that structured masking may produce more useful representations when evaluated directly (i.e., without fine-tuning), although these benefits do not necessarily transfer fully after model fine-tuning.

Table 15. **Evaluation of different choices of masking for MAE-B models across three datasets.** We report the weighted F1 score (%) on TreeSatAI-TS and the mIoU (%) on PASTIS-HD and FLAIR-HUB 20%.

Modality	Masking structure		TreeSatAI-TS	PASTIS-HD fold I	FLAIR-HUB filt. 20% / split 1
	Spatial	Temporal			
✓	✓	✓	<b>78.5</b>	<b>68.8</b>	<b>63.6</b>
✗	✓	✓	78.5	68.4	63.3
✓	✗	✓	78.5	68.6	63.0
✓	✓	✗	78.3	68.5	63.4
✗	✗	✗	78.2	68.4	63.6

Table 16. **Probing evaluation of different choices of masking for MAE-B models across three datasets.** We report the weighted F1 score (%) on TreeSatAI-TS and the mIoU (%) on PASTIS-HD and FLAIR-HUB 20%.

Modality	Masking structure		TreeSatAI-TS	PASTIS-HD fold I	FLAIR-HUB filt. 20% / split 1
	Spatial	Temporal			
✓	✓	✓	69.3	61.2	56.2
✗	✓	✓	69.8	61.4	56.3
✓	✗	✓	69.6	<b>61.5</b>	56.3
✓	✓	✗	69.2	57.7	56.2
✗	✗	✗	<b>69.9</b>	57.6	<b>56.3</b>

## 7.5. Importance of Multitemporal Components

We examine the impact of various multitemporal components on downstream task performance for MAE-B and ViT-B models. In these experiments, we use the *group* fusion mode, grouping together the Sentinel-1 ascending and descending modalities. For multispectral data, we use *joint-token* fusion combined with *patch-group-wise* target normalization during reconstruction.

We report in Tab. 17 the effect of varying the number of temporal bins  $D_m$  for the Sentinel-2 and Sentinel-1 ascending and descending modalities. Additionally, we show in Tab. 18 the impact of removing date encodings and disabling the data augmentation associated with random time step selection within temporal bins.

In Tab. 17, we observe that the choice of  $D_m$  for Sentinel-2 is critical when this modality drives performance, as in TreeSatAI-TS and PASTIS-HD (see Sec. 7.6). Notably, the performance gap between  $D_m = 16$  and  $D_m = 1$  for Sentinel-2 is much larger than that between  $D_m = 1$  and  $D_m = 0$ . This indicates that it is the multitemporal dynamics of Sentinel-2, rather than its monotemporal component, that is essential. In contrast, varying  $D_m$  for Sentinel-1 has only a minor effect, reflecting its smaller role (see Sec. 7.6).

In Tab. 18, we find that removing date encodings leads to a clear performance drop whenever multitemporal dynamics are important. Random time step selection during training generally improves performance, although the magnitude of its benefit varies across datasets.

Table 17. **Importance of the number of temporal bins for MAE-B and ViT-B models across three datasets.** We report the weighted F1 score (%) on TreeSatAI-TS and the mIoU (%) on PASTIS-HD and FLAIR-HUB 20%. Arrows ( $\uparrow$  /  $\downarrow$ ) indicate the difference compared to using 16 temporal bins for the Sentinel-2 modality and 4 temporal bins for the Sentinel-1 ascending and descending modalities.

Model	Number of temporal bins			TreeSatAI-TS	PASTIS-HD fold I	FLAIR-HUB filt. 20% / split 1
	S1 <sub>ASC</sub>	S1 <sub>DES</sub>	S2			
MAE	4	4	16	<b>78.5</b>	68.8	<b>63.6</b>
MAE	4	4	4	75.3 $\downarrow$ 3.2	64.3 $\downarrow$ 4.5	62.4 $\downarrow$ 1.2
MAE	4	4	1	73.1 $\downarrow$ 5.4	49.3 $\downarrow$ 19.5	61.8 $\downarrow$ 1.8
MAE	4	4	0	72.6 $\downarrow$ 5.9	44.9 $\downarrow$ 23.9	61.6 $\downarrow$ 2.0
MAE	1	1	16	78.3 $\downarrow$ 0.2	68.8 $\uparrow$ 0.0	63.5 $\downarrow$ 0.1
MAE	0	0	16	78.2 $\downarrow$ 0.3	<b>69.2</b> $\uparrow$ 0.4	63.1 $\downarrow$ 0.5
ViT	4	4	16	75.7	<b>64.6</b>	59.5
ViT	4	4	4	70.6 $\downarrow$ 5.1	61.2 $\downarrow$ 3.4	58.4 $\downarrow$ 1.1
ViT	4	4	1	66.1 $\downarrow$ 9.6	46.5 $\downarrow$ 18.1	57.6 $\downarrow$ 1.9
ViT	4	4	0	65.8 $\downarrow$ 9.9	41.5 $\downarrow$ 23.1	57.4 $\downarrow$ 2.1
ViT	1	1	16	<b>75.8</b> $\uparrow$ 0.1	64.6 $\uparrow$ 0.0	<b>59.8</b> $\uparrow$ 0.3
ViT	0	0	16	75.7 $\uparrow$ 0.0	64.4 $\downarrow$ 0.2	59.2 $\downarrow$ 0.3

Table 18. **Impact of removing date encodings and disabling random time step selection for MAE-B and ViT-B models across three datasets.** We report the weighted F1 score (%) on TreeSatAI-TS and the mIoU (%) on PASTIS-HD and FLAIR-HUB 20%. Arrows ( $\uparrow$  /  $\downarrow$ ) indicate the difference compared to including date encodings and enabling random time step selection.

Model	Number of temporal bins			Date encodings	Random time step selection	TreeSatAI-TS	PASTIS-HD fold I	FLAIR-HUB filt. 20% / split 1
	S1 <sub>ASC</sub>	S1 <sub>DES</sub>	S2					
MAE	4	4	16	✓	✓	78.5	<b>68.8</b>	63.6
MAE	4	4	16	✗	✓	77.5 $\downarrow$ 1.0	67.8 $\downarrow$ 1.0	63.6 $\uparrow$ 0.0
MAE	4	4	16	✓	✗	<b>78.8</b> $\uparrow$ 0.3	68.2 $\downarrow$ 0.6	<b>63.7</b> $\uparrow$ 0.1
ViT	4	4	16	✓	✓	<b>75.7</b>	<b>64.6</b>	<b>59.5</b>
ViT	4	4	16	✗	✓	74.8 $\downarrow$ 0.9	63.8 $\downarrow$ 0.8	59.4 $\downarrow$ 0.1
ViT	4	4	16	✓	✗	75.4 $\downarrow$ 0.3	63.9 $\downarrow$ 0.7	58.7 $\downarrow$ 0.8

## 7.6. Importance of each Modality by Dataset

We present an ablation study on modality removal for MAE-B and ViT-B models. Results are reported in Tab. 19. In these experiments, we use the *group* fusion mode, grouping together the Sentinel-1 ascending and descending modalities. For multispectral data, we use *joint-token* fusion along with *patch-group-wise* target normalization during reconstruction.

Table 19. **Impact of removing modalities for MAE-B and ViT-B models across three datasets.** We report the weighted F1 score (%) on TreeSatAI-TS and the mIoU (%) on PASTIS-HD and FLAIR-HUB 20%. Arrows ( $\uparrow$  /  $\downarrow$ ) indicate the difference compared to including all modalities.

Model	TreeSatAI-TS				PASTIS-HD fold I				FLAIR-HUB filt. 20% / split 1				
	Aerial	S1	S2	wF1 (%)	Spot	S1	S2	mIoU (%)	Aerial	S1	S2	DEM/DSM	mIoU (%)
MAE	✓	✓	✓	<b>78.5</b>	✓	✓	✓	68.8	✓	✓	✓	✓	<b>63.6</b>
MAE	✗	✓	✓	76.8 $\downarrow$ 1.7	✗	✓	✓	68.6 $\downarrow$ 0.2	✗	✓	✓	✓	52.2 $\downarrow$ 11.4
MAE	✓	✗	✓	78.2 $\downarrow$ 0.3	✓	✗	✓	<b>69.2</b> $\uparrow$ 0.4	✓	✗	✓	✓	63.1 $\downarrow$ 0.5
MAE	✓	✓	✗	72.6 $\downarrow$ 5.9	✓	✓	✗	44.9 $\downarrow$ 23.9	✓	✓	✗	✓	61.6 $\downarrow$ 2.0
MAE									✓	✓	✓	✗	62.7 $\downarrow$ 0.9
ViT	✓	✓	✓	<b>75.7</b>	✓	✓	✓	<b>64.6</b>	✓	✓	✓	✓	<b>59.5</b>
ViT	✗	✓	✓	75.3 $\downarrow$ 0.4	✗	✓	✓	64.5 $\downarrow$ 0.1	✗	✓	✓	✓	47.9 $\downarrow$ 11.6
ViT	✓	✗	✓	75.7 $\uparrow$ 0.0	✓	✗	✓	64.4 $\downarrow$ 0.2	✓	✗	✓	✓	59.2 $\downarrow$ 0.3
ViT	✓	✓	✗	65.8 $\downarrow$ 9.9	✓	✓	✗	41.5 $\downarrow$ 23.1	✓	✓	✗	✓	57.4 $\downarrow$ 2.1
ViT									✓	✓	✓	✗	58.3 $\downarrow$ 1.2

We observe that both MAEs and ViTs generally perform best when all modalities are included. The Sentinel-2 modality has a strong influence on tasks heavily tied to multitemporal dynamics, such as tree species identification and crop segmentation. Additionally, the modality from which the ground truth is derived markedly affects performance—for example, aerial imagery for FLAIR-HUB and Sentinel-2 for PASTIS-HD.

The slight performance drop observed when omitting Sentinel-1 on PASTIS-HD may stem from the combination of two factors: (i) its lower task relevance compared to Sentinel-2, and (ii) the relatively shallow segmentation heads, which aggregate multimodal and multitemporal features via a single attentive pooling and may struggle to suppress irrelevant features, thereby introducing noise into the predictions.

## 8. Inference Results

In this section, we report examples of inference results from MAESTRO and supervised ViTs on the segmentation tasks of PASTIS-HD and FLAIR-HUB. We again consider MAESTRO and ViTs with the *group* fusion mode, grouping together the Sentinel-1 ascending and descending modalities. For multispectral data, we use *joint-token* fusion along with *patch-group-wise* target normalization during reconstruction.

Results are reported in Fig. 7 and Fig. 8 for PASTIS-HD and FLAIR-HUB, respectively. For each tile, we display the VHR imagery, the Sentinel-2 imagery, the MAESTRO prediction, the ViT prediction, and the corresponding ground truth. Examples are randomly sampled from the test set.

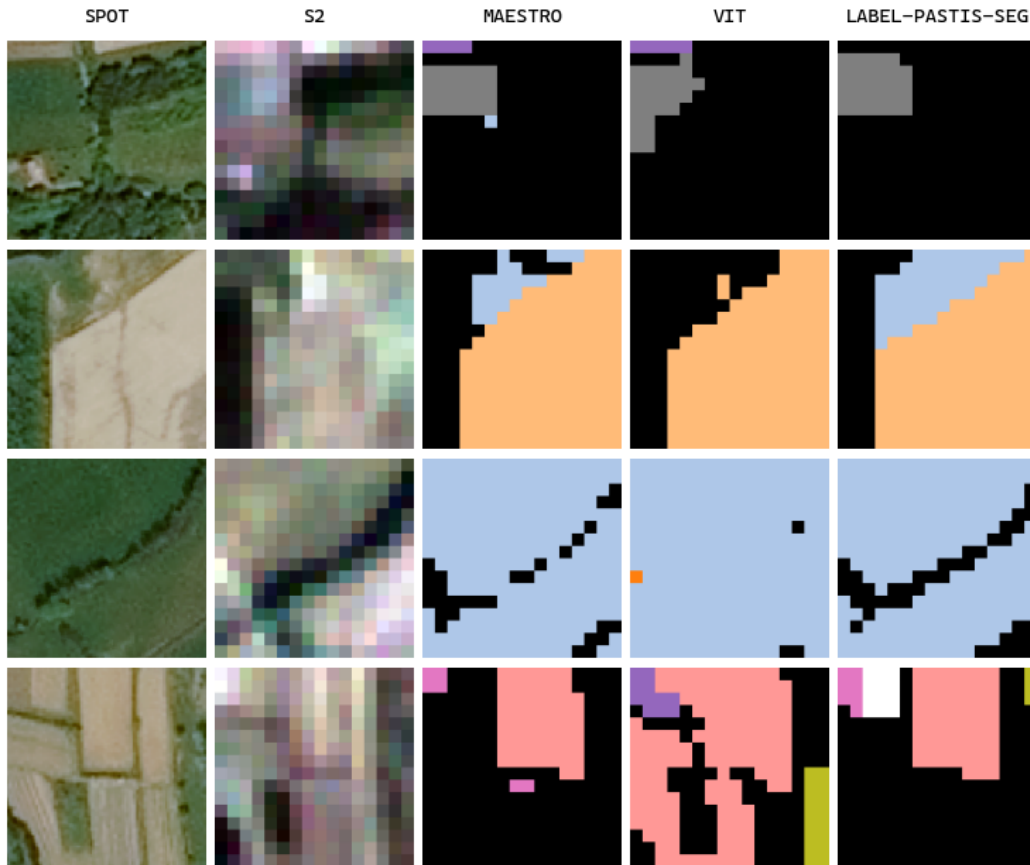


Figure 7. **Inference results from MAESTRO-B and ViT-B models on PASTIS-HD.** For Sentinel-2 imagery, we report the pixel-wise median across temporal bins. White parcels correspond to areas with missing annotations (void labels).

In Fig. 7, MAESTRO produces precise segmentation masks on PASTIS-HD, closely matching the boundaries of parcel and tree-covered areas. Its predictions are more spatially coherent than those of ViTs and better differentiate crop types.

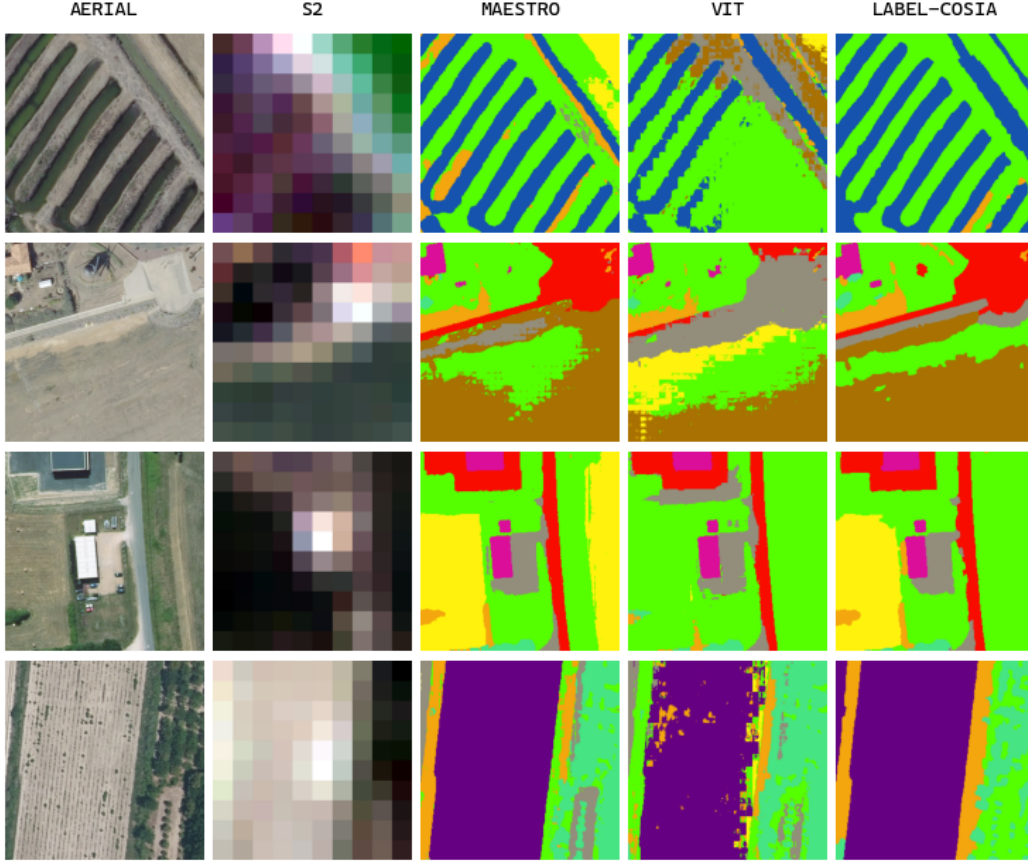


Figure 8. **Inference results from MAESTRO-B and ViT-B models on FLAIR-HUB.** For Sentinel-2 imagery, we report the pixel-wise median across temporal bins.

In Fig. 8, although the complex scenes in FLAIR-HUB introduce prediction ambiguities, MAESTRO still delivers sharper and more accurate object delineations than ViTs. It also performs better on classes such as brushwood and water, and more effectively separates impervious from pervious surfaces.

## 9. Computational Costs

In this section, we quantify floating-point operations (FLOPs) (Sec. 9.1) and report the overall computational cost of the experiments shown in the paper (Sec. 9.2).

### 9.1. MACs/FLOPs

We report FLOPs per forward pass separately for SSL pre-training (Sec. 9.1.1) and probing/fine-tuning (Sec. 9.1.2). While forward FLOPs are identical between probing and fine-tuning, probing is substantially more efficient when backward FLOPs are taken into account.

Forward FLOPs (for a single batch element) are computed for MAESTRO-B, MAE-B, and ViT-B models. We first calculate the number of multiply-accumulate operations (MACs), then convert to FLOPs using the relation  $\text{FLOPs} = 2 \times \text{MACs}$ . Following standard practice, we include only operations from model components with significant MAC contributions, excluding element-wise operations such as normalizations, nonlinearities, biases, and component-wise summations.

We again consider the *group* fusion mode, grouping the Sentinel-1 ascending and descending modalities together. For multispectral data, we evaluate both *joint-token* and *token-based* multispectral fusion.



### 9.1.1. Pre-training MACs/FLOPs

For each modality  $m$ , let  $L_m$  denote its sequence length. With *joint-token* multispectral fusion, the sequence length is  $L_m = (I_m/P_m)^2 D_m$ , where  $I_m$  is the image size,  $P_m$  the patch size, and  $D_m$  the number of temporal bins. With *token-based* multispectral fusion, the sequence length becomes  $L_m = (I_m/P_m)^2 D_m |\mathcal{G}_m|$ , where  $|\mathcal{G}_m|$  is the cardinality of the set of band groups mapped to different tokens.

For a modality  $m$  that is not grouped with others via early multimodal fusion, the MACs in the *encoder* and *decoder* are:

$$\begin{aligned} \text{MACs}^{\text{enc}} &= (12 \lfloor (1-M)L_m \rfloor C_e^2 + 2 \lfloor (1-M)L_m \rfloor^2 C_e) N_e, \\ \text{MACs}^{\text{dec}} &= (12 L_m C_d^2 + 2 L_m^2 C_d) N_d, \end{aligned}$$

where  $M$  is the fraction of masked tokens,  $N_e$  and  $N_d$  are the number of layers in the encoder and decoder, while  $C_e$  and  $C_d$  are the latent dimensions in the encoder and decoder.

For the grouped Sentinel-1 ascending and descending modalities,  $\text{MACs}^{\text{enc}}$  and  $\text{MACs}^{\text{dec}}$  are computed by replacing  $L_m$  with the *sum of sequence lengths* of the two modalities.

The *dense* layers that project from the encoder space to the decoder space contribute:

$$\text{MACs}^{\text{enc-to-dec}} = \sum_m \lfloor (1-M)L_m \rfloor C_e C_d.$$

The *patchify* and *unpatchify* operations contribute:

$$\begin{aligned} \text{MACs}^{\text{patchify}} &= \sum_m I_m^2 D_m C_m C_e, \\ \text{MACs}^{\text{unpatchify}} &= \sum_m I_m^2 D_m C_m C_d, \end{aligned}$$

where  $C_m$  is the number of channels for each modality  $m$ .

Putting everything together, and using  $M = 0.75$  for the fraction of masked tokens,  $N_e = 12$ ,  $C_e = 768$  for the encoder, and  $N_d = 3$ ,  $C_d = 512$  for the decoder, we compute the forward MACs/FLOPs for MAESTRO-B and MAE-B models during pre-training, based on the default configurations in Tab. 5, Tab. 6, and Tab. 7. This computation is carried out for both *joint-token* and *token-based* multispectral fusion across the four evaluated datasets. Results are reported in Tab. 20.

Table 20. **MACs/FLOPs for MAESTRO-B and MAE-B models during pre-training.** We report the forward MACs/FLOPs (for a single batch element) for both joint-token and token-based multispectral fusion across the four evaluated datasets. Multipliers (x) indicate the FLOPs increase compared to using joint-token multispectral fusion.

Multispectral fusion	TreeSatAI-TS		PASTIS-HD		FLAIR#2		FLAIR-HUB	
	MACs ( $\times 10^9$ )	FLOPs ( $\times 10^9$ )	MACs ( $\times 10^9$ )	FLOPs ( $\times 10^9$ )	MACs ( $\times 10^9$ )	FLOPs ( $\times 10^9$ )	MACs ( $\times 10^9$ )	FLOPs ( $\times 10^9$ )
Joint-token	14.3	28.7	56.1	112.1	59.1	118.2	65.4	130.9
Token-based	33.7 $\times 2.4$	67.4 $\times 2.4$	173.6 $\times 3.1$	347.2 $\times 3.1$	133.9 $\times 2.3$	267.8 $\times 2.3$	146.9 $\times 2.2$	293.8 $\times 2.2$

### 9.1.2. Probing/Fine-tuning MACs/FLOPs

We reuse the same notation as in Sec. 9.1.1. As before, the sequence length is given by  $L_m = (I_m/P_m)^2 D_m$  for *joint-token* multispectral fusion, and by  $L_m = (I_m/P_m)^2 D_m |\mathcal{G}_m|$  for *token-based* multispectral fusion.

For a modality  $m$  that is not grouped with others via early multimodal fusion, the MACs in the *encoder* are:

$$\text{MACs}^{\text{enc}} = (12 L_m C_e^2 + 2 L_m^2 C_e) N_e.$$

For the grouped Sentinel-1 ascending and descending modalities,  $\text{MACs}^{\text{enc}}$  is computed by replacing  $L_m$  with the *sum of sequence lengths* of the two modalities.

The attentive pooling operations in the classification and segmentation heads contribute:

$$\text{MACs}^{\text{attn-pool}} = 2 \sum_m L_m C_e.$$

The final *dense* projections in the classification and segmentation heads contribute:

$$\begin{aligned}\text{MACs}^{\text{proj-cls}} &= C_e C_{\text{cls}}, \\ \text{MACs}^{\text{proj-seg}} &= L_{\text{ref}} C_e C_{\text{seg}},\end{aligned}$$

where  $L_{\text{ref}}$  is the sequence length of the spatial *token grid of reference* (see Sec. 3.3), while  $C_{\text{cls}}$  and  $C_{\text{seg}}$  are the number of semantic classes for the classification and segmentation tasks, respectively, including the classes ignored during loss and metric computations (see Sec. 6.1).

Putting everything together, and using  $N_e = 12$ ,  $C_e = 768$  for the encoder, we compute the forward MACs/FLOPs for MAESTRO-B, MAE-B, and ViT-B models during probing/fine-tuning, based on the default configurations in Tab. 5, Tab. 6, and Tab. 7. This computation is performed for both *joint-token* and *token-based* multispectral fusion across the four evaluated datasets. The results are presented in Tab. 21.

Table 21. **MACs/FLOPs for MAESTRO-B, MAE-B, and ViT-B models during probing/fine-tuning.** We report the forward MACs/FLOPs (for a single batch element) for both joint-token and token-based multispectral fusion across the four evaluated datasets. Multipliers (x) indicate the FLOPs increase compared to using joint-token multispectral fusion.

Multispectral fusion	TreeSatAI-TS		PASTIS-HD		FLAIR#2		FLAIR-HUB	
	MACs ( $\times 10^9$ )	FLOPs ( $\times 10^9$ )	MACs ( $\times 10^9$ )	FLOPs ( $\times 10^9$ )	MACs ( $\times 10^9$ )	FLOPs ( $\times 10^9$ )	MACs ( $\times 10^9$ )	FLOPs ( $\times 10^9$ )
Joint-token	39.1	78.3	163.4	326.8	167.4	334.8	185.1	370.3
Token-based	95.0 $\times 2.4$	190.0 $\times 2.4$	549.9 $\times 3.4$	1099.9 $\times 3.4$	403.9 $\times 2.4$	807.8 $\times 2.4$	440.8 $\times 2.4$	881.7 $\times 2.4$

## 9.2. Overall Computational Cost

All our experiments were run on SLURM clusters, with either V100, A40, A100, or H100 GPU nodes. Training was performed in mixed precision.

In total, running all the experiments shown in the paper required 17 661 V100 hours, 7 736 A40 hours, 268 A100 hours, and 268 H100 hours.